A GRANULAR FLOW MODEL FOR DEVELOPING SMART ARMOR CERAMICS

FINAL TECHNICAL REPORT

RICHARD W. KLOPP, RESEARCH ENGINEER III
DONALD A. SHOCKEY, ASSOCIATE DIRECTOR
DONALD R. CURRAN, SENIOR STAFF SCIENTIST
THOMAS COOPER, RESEARCH ENGINEER

JANUARY 31, 1998

U.S. ARMY RESEARCH OFFICE

CONTRACT NO. DAAH04-94-K-0001

SRI INTERNATIONAL

APPROVED FOR PUBLIC RELEASE;
DISTRIBUTION UNLIMITED

THE VIEWS, OPINIONS, AND/OR FINDINGS CONTAINED IN THIS REPORT ARE
THOSE OF THE AUTHOR(S) AND SHOULD NOT BE CONSTRUED AS AN
OFFICIAL DEPARTMENT OF THE ARMY POSITION, POLICY, OR DECISION,
UNLESS SO DESIGNATED BY OTHER DOCUMENTATION.

19991215 032

REPORT DOCUMENTATION PAGE

1. AGENCY USE ONLY (Leave Blank)	2. REPORT DATE 31 January 1998	3. REPORT TYPE AND DATES COVERED Final Report 29 Aug 94 - 31 Dec 97

4. TITLE AND SUBTITLE

A Granular Flow Model for Developing Smart Armor Ceramics

5. FUNDING NUMBERS

DAAH04-94-K-0001

6. AUTHOR(S)

R. W. Klopp, D. A. Shockey, D. R. Curran, and T. Cooper

7. PERFORMING ORGANIZATION NAME(S) AND ADDRESS(ES)

SRI International
333 Ravenswood Avenue
Menlo Park, CA 94025-3493

8. PERFORMING ORGANIZATION REPORT NUMBER

PO 6188

9. SPONSORING / MONITORING AGENCY NAME(S) AND ADDRESS(ES)

U.S. Army Research Office
Post Office Box 12211
Research Triangle Park, NC 27709-2211

10. SPONSORING / MONITORING AGENCY REPORT NUMBER

ARo 30330.2-MS

11. SUPPLEMENTARY NOTES

The views, opinions and/or findings contained in this report are those of the author(s) and should not be construed as an official Department of the Army position, policy, or decision, unless so designated by other documentation.

12a. DISTRIBUTION / AVAILABILITY STATEMENT

Approved for public release; distribution unlimited.

12b. DISTRIBUTION CODE

13. ABSTRACT (Maximum 200 words)

SRI International modeled the comminution and flow of ceramic under conditions like those in ceramic armor at the nose of an advancing penetrator. We delivered a model, FRAGBED2, that models fracture, comminution, compaction, and fragment flow, and can be implemented in hydrocodes. Fragment motion is treated by analogy with atomic dislocation theory. Compaction occurs by the outflow of dislocation holes. The rate of comminution is zero below a threshold stress and saturates above a saturation stress, and varies smoothly in between.

We tested FRAGBED2 by comparing results from three types of experiments: spherical cavity expansion tests, thick-walled cylinder collapse tests, and ballistic tests. In the cavity expansion tests, an explosion in a spherical cavity machined in a block of ceramic produced a distribution of fragment sizes as a function of distance. From the distribution, we obtained parameters for calibrating the comminution model. The thick-walled cylinder test was modified by introducing a taper that allowed a complete range of strains to be produced. Extensive shear banding was observed in recovered specimens, which FRAGBED2 was not able to model in 2-D plane strain. However, FRAGBED2 did a good job of matching the ballistic test results.

14. SUBJECT TERMS

ceramic armor, fragment flow model, comminution, dislocation model, spherical cavity expansion, thick-walled cylinder method, penetration model, ballistic impact, alumina

15. NUMBER OF PAGES

90

16. PRICE CODE

17. SECURITY CLASSIFICATION OF REPORT	18. SECURITY CLASSIFICATION OF THIS PAGE	19. SECURITY CLASSIFICATION OF ABSTRACT	20. LIMITATION OF ABSTRACT
UNCLASSIFIED	UNCLASSIFIED	UNCLASSIFIED	UL

CLASSIFIED BY :

DECLASSIFY ON :

CONTENTS

ILLUSTRATIONS

TABLES

viii

EXECUTIVE SUMMARY

SRI International modeled the comminution and flow of ceramic under conditions like those in ceramic armor at the nose of an advancing penetrator. We have delivered a model, FRAGBED2, that models fracture, comminution, compaction, and fragment flow, and can be implemented in hydrocodes. Fragment motion is treated by analogy with atomic dislocation theory. That is, blocky fragments are imagined to glide in small increments along fixed planes in the material. As fragments flow one way, lines of holes flow the other way. Compaction occurs by the outflow of holes, and dilatancy occurs by the influx of holes, and dilatancy occurs by the influx of holes. Comminution is treated by an "overstress" type of rate model. The rate of comminution is zero below a threshold stress, saturates above a saturation stress, and varies smoothly in between.

FRAGBED2 is an improvement over models used presently for armor simulations because it captures the relevant physics. FRAGBED2 parameters are directly related to readily measured material properties, such as the fracture toughness, friction coefficient, relative size of pre-existing flaws, density, and porosity.

We tested FRAGBED2 by comparing results from three types of experiments: spherical cavity expansion tests, thick-walled cylinder collapse tests, and ballistic tests. In the cavity expansion tests, an explosive charge in a spherical cavity machined in a split block of ceramic produced a distribution of fragment sizes as a function of distance. By examining the distribution posttest, we obtained parameters for calibrating the comminution model. The thick-walled cylinder test, conceived by Nesterenko, was modified by introducing a taper that allowed a complete range of strains to be produced. Extensive shear banding was observed in recovered specimens. Two-dimensional hydrocode simulations with FRAGBED2 were able to model the final deformation of the cylinder, but were not able to model the observed shear banding. We found that three-dimensional flow in the specimen makes it difficult to compare these experimental results with the results of two-dimensional calculations. Thus, three-dimensional hydrocode calculations probably will be required to test the ability of FRAGBED2 to model shear banding. FRAGBED2 did a good job of matching the ballistic test results. The experimental results were for long-rod penetrations into alumina ceramic, and were obtained from the literature.

SECTION 1
INTRODUCTION AND BACKGROUND

SRI International modeled the comminution and flow of ceramic under conditions like those in ceramic armor at the nose of an advancing penetrator. Penetrating weapons or explosive charges in brittle materials such as ceramics, concrete, or hard rock, produce fracture and fragmentation near the cavity boundary to form a bed of fragmented or granulated material. Penetration occurs by further comminution of the material into a finely granulated bed (called the Mescall zone) and the subsequent flow of the granules out of the way of the advancing penetrator [1], as shown schematically in Figure 1. In quasi-static and dynamic tests under conditions of compression and shear, the yielding behavior of brittle frictional materials can be interpreted as the result of frictional sliding of debonded granules. Thus, modeling the formation and flow of a granulated bed is key to computing cratering and penetration in brittle materials, and to interpreting laboratory tests of such materials.
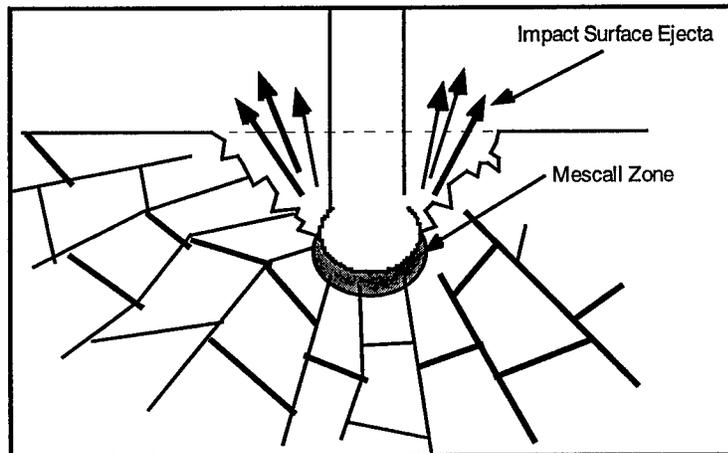
Figure 1. Damage pattern in ceramic during long-rod penetration.

In a prior paper [2], we presented a granulated material model for use in finite element hydrocodes applied to penetration of ceramic armors or hard rock. The model, named FRAGBED, included a mesomechanical description of shear flow and associated dilatancy. It is a non-local, multiplane, plasticity model (see, for example, Batdorf and Budianski [3], Curran et al. [4], and Bazant et al. [5]) that proved useful in computational simulations and associated interpretations of penetration experiments in which ceramic armors were attacked by long-rod penetrators [1].

However, a drawback to FRAGBED was that the pore compaction was handled from a continuum viewpoint, whereas the shear flow and associated dilatancy were treated from a mesomechanical viewpoint. In fact, both dilatancy and pore compaction arise from the same mesomechanical processes. In addition, the important process of granule comminution was not treated in FRAGBED, and the fracture processes that initially produce the fragmented bed were treated only cursorily.

We expanded the FRAGBED model to be a complete micromodel for the fracture, fragmentation, comminution, shear flow, dilatancy, and pore compaction processes in ceramics. We call this expanded model FRAGBED2, and the original model FRAGBED1.

SECTION 2

APPROACH

The FRAGBED models are mesomechanical and average the behavior inside a relevant volume element (RVE), as discussed by Curran et al. [4], Bazant [5], Nemat-Nasser [6], and numerous other authors. The RVE must contain many granules. As described in [2], the FRAGBED approach to modeling the flow of granulated material is to focus not on the granules themselves, but rather on the holes between the granules. Figure 2 provides a schematic view of this approach.

By analogy to atomic dislocation theory, a hole large enough to allow sliding of a granule into it is called a vacancy, and strings of such holes are called dislocations. Just as for the atomic case, the dislocations can be mobile or pinned, will have edge and screw components, and can glide or climb. The dislocations can become pinned when obstacles stop their motion, and can later become unpinned by granule rearrangement. As discussed in [2], this analogy is useful because it allows us to easily relate non-elastic slip in the granular bed to macroscopic plastic strain rate. By casting the model in the framework of multiplane plasticity theory, the analogy between granular flow and slip in single crystals is direct, and many of the techniques and results of the community engaged in mesomechanical modeling of crystalline plasticity can be applied. We can thus use terms commonly associated with atomic dislocation theory to refer to granular flow processes.

Before the dislocation analogy can be applied, the material must be converted from an intact material to a fragmented bed. FRAGBED1 currently uses a very simple damage evolution algorithm based on a combination of tensile and shear strains. When the damage function attains a critical value, the material cohesion and tensile strength reach zero and the material element is declared fragmented. Thereafter the fragmented bed model is used, with the average fragment size and dislocation density specified as input constants.

In FRAGBED2 we introduced three changes. First, FRAGBED2 provides a simple model of the coalescence of cracks nucleated at flaws to form an initial granule size distribution (FRAGBED1 assumed a constant initial granule size; this option remains available in FRAGBED2). However, this initial fragmentation algorithm remains very approximate. The
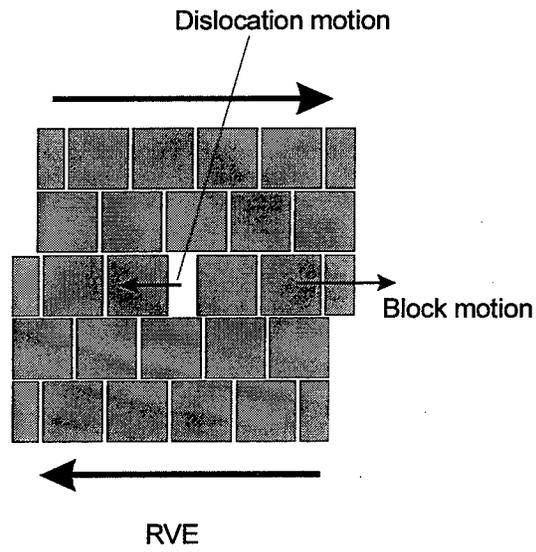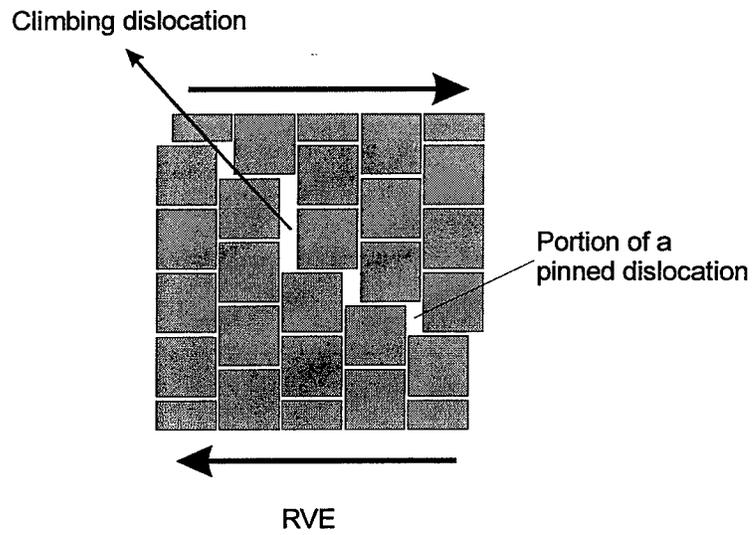
Figure 2. FRAGBED2 dislocation analogy.
(a) Case I - unimpeded motion. (b) Case II - impeded motion.
(c) Definition of parameters. (continued)
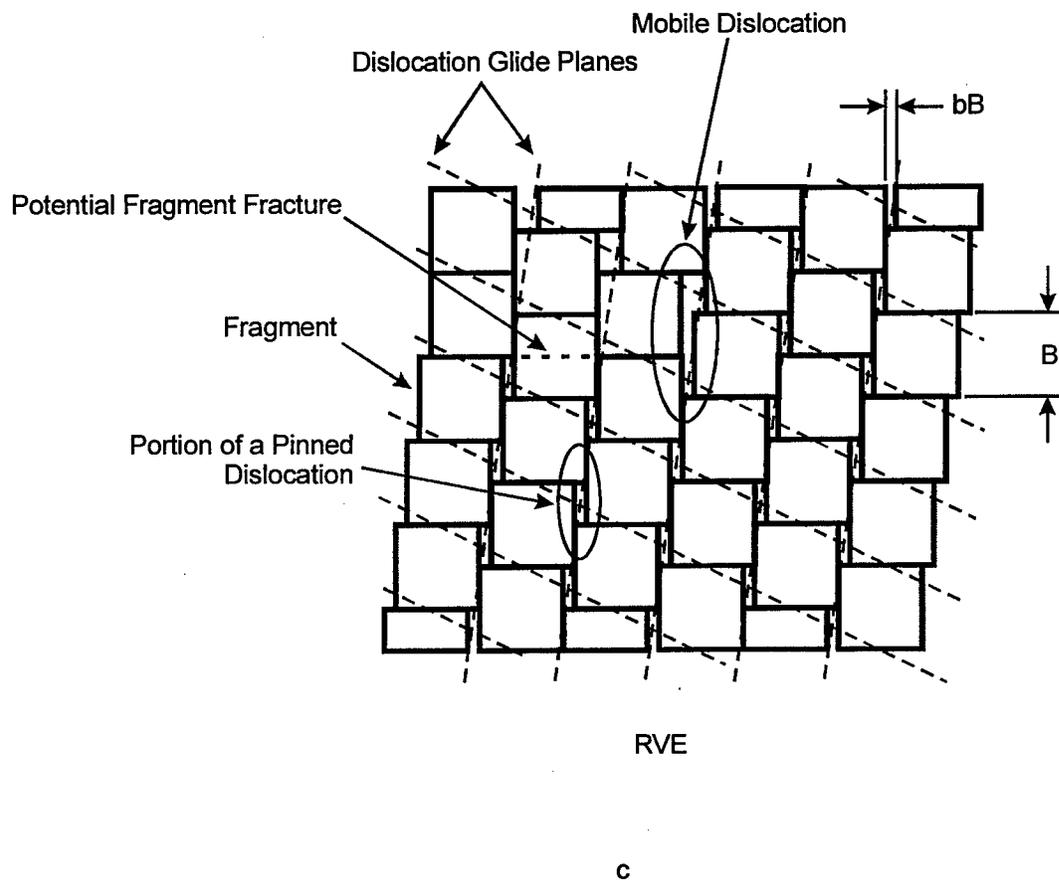
Figure 2. FRAGBED2 dislocation analogy.
(a) Case I - unimpeded motion. (b) Case II - impeded motion.
(c) Definition of parameters. (concluded)

second change was to introduce evolution equations for the average fragment size and the dislocation density, i.e., we introduced a comminution model. The third change was to introduce a micromechanical model for porosity evolution. This model replaced the dilatancy model and the continuum model for compaction used in FRAGBED1. Both the dilatancy and pore compaction are a consequence of dislocation flux across the boundary of the RVE; dilatancy is caused by dislocations flowing into the RVE, whereas compaction is caused by dislocations flowing out of the RVE.

SECTION 3
DESCRIPTION OF FRAGBED2

FRACTURE AND FRAGMENTATION PROCESS

We assume that initially intact brittle material is converted to a fragmented bed by the activation, growth, and intersection of cracks that initiate at inherent flaws in the material. For example, in an initially intact ceramic under compressive and shear stresses, one could imagine that the flaws, which may consist of relatively weak grain boundaries, microcracks, or other stress raisers, will become active when the shear stresses exceed the cohesion, or when local anisotropy and inhomogeneity cause local tensile stresses even under global compression. [Under uniaxial strain conditions, this would occur at the Hugoniot elastic limit (HEL)]. In a jointed hard rock formation, the same process could occur under compressive and shear loads that vary slowly over the scale of the joint spacing. For common ceramics or intact hard rock, this will require compressive stresses on the order of 10 GPa, but would occur at much lower pressures for heavily jointed, weakly cemented rock. For the ceramic penetration and tapered cylinder experiments to be discussed later, we assume that the primary fragmentation process near the nose of the penetrator and in the tapered cylinder is grain boundary debonding. Thus, the initial fragment size distribution is that of the ceramic grains. (In these cases, significant shear flow occurs, and it is the fragment sizes of the flowing material that are relevant.)

For cavity expansion experiments, although the above compression and shear process will occur in the immediate vicinity of the cavity boundary, the fragmentation process farther from the cavity boundary occurs via the intersection of tensile cracks. These tensile cracks are nucleated by the spherically divergent shock wave, which produces tensions normal to the direction of propagation. These larger fragments exhibit negligible shear flow. We next develop a simple algorithm for this fragmentation process.

A complete description of this process would begin by using a mesomechanical model such as that of Simons et al. for concrete [7], to calculate the fragment pattern. For a recent review of such approaches, see Rajendran [8]. However, we postpone such complexity by using a simple algorithm as a preprocessor to establish the initial fragmented bed, as discussed below.

7

In cases of penetration or cratering, we observe experimentally that cone cracks radiate into the target, and these are intercepted by spoke cracks. The spoke cracks are sketched in Figure 3. The shaded region is the loaded region, or cavity. Both spoke and cone cracks arise from membrane tensions produced by the spherically divergent shock wave and associated particle velocity field. Surface observations commonly show many such cracks near the load center and fewer cracks at relatively large distances from the center.
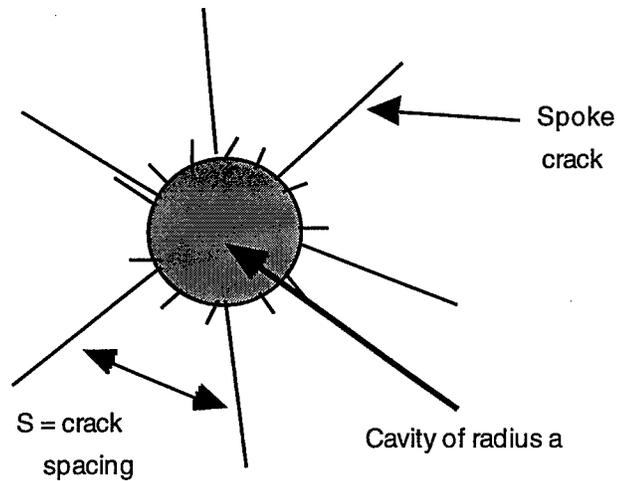
Figure 3. Radial spoke crack pattern on surface of brittle target.

The compressive stress in the shock propagation direction is followed by tesions that can cause lateral cracks that intersect the spoke and cone cracks to produce a fragmented bed. Also, the spoke and cone cracks branch and meander to intersect and form fragments.

The divergent shock wave will produce high hoop tensions at high strain rates ($>10^4$ s^{-1}) in the target material near the load center. These tensions will initiate many spoke and cone cracks, and their average spacing can be estimated with the Grady algorithm (for a recent review, see [9]) for brittle material:

$$S \approx 3\left[\frac{K_c}{\rho c}\left(\frac{\partial \varepsilon}{\partial t}\right)^{-1}\right]^{2/3} \tag{3-1}$$

where S is the crack spacing, K_C is the fracture toughness, ρ is the density, $\partial \varepsilon/\partial t$ is the continuum strain rate at the time of fracture, and c is the longitudinal sound speed.

The strain rate of interest is the rate at which the material is stretching in the membrane direction in the shock pulse, which is given by

$$\frac{\partial \varepsilon}{\partial t} \approx \frac{u}{r} \tag{3-2}$$

where u is the radial particle velocity and r is the distance from the impact site. We obtain u from the jump condition

$$u = \frac{P}{\rho c} \tag{3-3}$$

where P is the compressive shock stress and c is the shock velocity. Combining Eqs. (1) - (3) yields

$$S \approx \left(\frac{5rK_c}{P}\right)^{2/3} \tag{3-4}$$

The shock pressure in an elastic fluid decays according to the equation

$$P = P_0 \frac{a}{r} \tag{3-5}$$

where a is the initial cavity radius, which we can approximate with the penetrator radius, and P_0 is the impact pressure. Combining Eqs. (4) and (5), and setting S equal to the initial fragment size, B_0, yields

$$B_0 \approx \left(\frac{5K_c}{P_0 a}\right)^{2/3} r^{4/3} \qquad (3\text{-}6)$$

As discussed later, in modeling the cavity expansion test, we used the above equation to create the initial fragmented bed before we began the hydrocode simulations. We adjusted the comminution parameters to match experimental observations. Thus, although Eqs. (3-6) give initial sizes somewhat larger than the grain sizes, the comminution process soon reduces the sizes to below the average grain size.

COMMINUTION PROCESS

We return to the simplified picture of the fragmented bed discussed in [2], as shown in Figure 2. We assume an initial size distribution of fragments, idealized here as equisized square blocks.

A key result of confinement at boundaries is that dislocation flux across material element boundaries is decreased, thereby inhibiting non-elastic flow of the fragmented bed. Perfect confinement would in fact prevent long-rod penetration of a ceramic target because, although the fragmented bed could flow slightly into any initial porosity, the granules would ultimately have no place to go.

We next consider the comminution of the initial fragment bed of Figure 2. We assume that the comminution process mainly consists of blocks pushing on each other to produce local shear and tensile stresses that in turn cause the blocks to fracture.

Figure 2 shows that fracture of a single block to form two smaller blocks causes the small holes above and to the right of the fractured block to become a single dislocation (a dislocation is a line of holes big enough to allow non-elastic block motion), because as the top part of the fractured block moves it produces a hole twice as big to its left, thereby allowing the full-sized blocks to move. The lower part of the fractured block moves to the left at the same time to form a right-moving dislocation. Thus, the fracture of the block nucleates a pair of edge dislocations

traveling in opposite directions, and the dislocation nucleation rate is directly tied to the comminution rate.

If all the Case II blocks were to break in two in the same manner, the situation would become that of Case I, with no block interference, but with twice the number of dislocations. In all cases, the nucleation process as such does not cause increased porosity (the hole area to volume ratio remains the same). A generalization of this process will be discussed later.

DILATANCY AND PORE COMPACTION PROCESSES

The internal dislocations in Figure 2 move up and left and down and right to cross the RVE boundaries, and result in the hole closures and associated compaction. At the same time, dislocations from adjacent RVEs may move into the RVE, resulting in dilatancy. Thus, the dilatancy or pore compaction is a result of the net flux of dislocations across RVE boundaries. This process will be discussed in more detail in Section 4.

SECTION 4

EVOLUTION EQUATIONS

NON-ELASTIC SLIP

As discussed in [2], the Orowon [10] equation is used on each slip plane. That is, on the ith slip plane,

$$\frac{\partial \gamma_i^p}{\partial t} = g_i N_{di} b_i B_i v_{di} = g_i N_{di} B_i v_{bi} \tag{4-1}$$

where γ_i^p is the non-elastic (plastic) slip strain on the ith plane, N_{di} is the mobile dislocation density on that plane, B_i is the block (granule) size in the direction of slip, $b_i B_i$ is the size of the dislocation hole in the direction of slip (a sort of macro Burger's vector), v_{di} is the dislocation velocity, v_{bi} is the corresponding block velocity, and g_i is a variable coefficient that depends on granule geometry. A detailed discussion is given in [2].

As in [2], the total strain rate on a slip plane is the sum of the elastic and non-elastic rates:

$$\frac{\partial \gamma_i}{\partial t} = \frac{1}{2G}\left(\frac{\partial \tau_i}{\partial t}\right) + \frac{\partial \gamma_i^p}{\partial t} \tag{4-2a}$$

$$\frac{\partial \varepsilon_v}{\partial t} = -\frac{1}{K(1-\phi)}\left(\frac{\partial P}{\partial t}\right) + \frac{\partial \phi}{\partial t} \tag{4-2b}$$

where the porosity $\phi = \sum_i \phi_i$ (see later discussion), γ_i is the total shear strain on the ith plane, τ_i is the resolved macroscopic shear stress across the plane, ε_v is the total volumetric strain, P is the pressure in the porous material, ϕ_i is the porosity (the ratio of void volume to total volume) associated with the ith plane, and G and K are the shear and bulk moduli of the intact material,

respectively. The division by $(1-\phi)$ in the first term on the right-hand side (rhs) of (2b) is based on the assumption of a partial pressure relationship:

$$P = (1-\phi)P_s \qquad (4\text{-}2c)$$

where P_s is the compressive mean stress in the intact material. We have also neglected terms of the order of $P_s/K(1-\phi)$. In the applications to be discussed, the porosity is restricted to a few percent by comminution and associated compaction, and this approximation is justified. Our model is not suitable in any case for large porosity, because in that event the dislocation approach appears unrealistic.

POROSITY

We assume for simplicity that all porosity is associated with dislocations. The total porosity ϕ is defined as the sum of the porosities ϕ_i associated with each plane, where ϕ_i is defined as the ratio of void volume associated with slip on the i th plane to the total volume. To simplify the notation, the i subscript will be dropped in further equations, and the equations will be assumed to refer to the i th plane unless otherwise specified. Thus, the value of porosity on each slip plane associated with N_d mobile dislocations per unit area is

$$\phi = nN_d bB^2 \qquad (4\text{-}3)$$

where we have approximated the individual mobile dislocation area as nbB^2, where n in Figure 2 is unity. For more realistic fragmented bed geometries than those of Figure 2, we can expect n to be greater than unity to allow unimpeded block motion. We have arbitrarily chosen $n = 3/2$.

The porosity can change only by hole migration across a material element boundary (dislocation flux). That is, as discussed in [2], the non-local nature of FRAGBED arises from the choice of a control volume (RVE) that contains many granules and associated dislocations. Applying the divergence theorem to the dislocation density for this control volume yields (on a single slip plane)

$$\frac{dN_d}{dt} = \frac{\partial N_{dn}}{\partial t} - \frac{\partial (N_d v_d)}{\partial x} \qquad (4\text{-}4)$$

where the first term on the right refers to the net nucleation rate of mobile dislocations (the nucleation rate minus the pinning rate), and the second term on the right refers to the net flux of dislocations across the surface of the material element. As seen in Figure 2, the nucleation and pinning processes do not change the porosity. Thus, only the second term on the right of Eq. (4-5) is used to obtain the evolution relation for the porosity, and for constant b and B

$$\left(\frac{\partial \phi}{\partial t}\right)_{x,b,B} = -\frac{3}{2}bB^2 \frac{\partial (N_d v_d)}{\partial x} \qquad (4\text{-}5)$$

where x is in the direction of slip on the i th plane.

The parameter b is important because it helps determine the porosity through Eq. (4-5). Its value is determined physically by the granule geometry and configurations. In the current form of FRAGBED2, however, the value of b is simply taken to be an adjustable constant with magnitude between zero and unity. (A value larger than unity would mean that the dislocation jog would be greater than the granule size.)

GRANULE AND DISLOCATION VELOCITIES

We also need an equation for the dislocation velocity, which is in turn related to the granule velocity [see Eq. (4-1)]. We can obtain the form of the equation from the simplified picture of Figure 2. Consider a cubic block of size B undergoing shear stress τ across an interface that may produce a slip in the x direction. The frictional resistance to slip is $\mu \sigma_n$. The impulse-momentum relation is

$$(\tau - \mu \sigma_n)B^2 dt = \rho_s B^3 dv \qquad (4\text{-}6a)$$

where μ is the coefficient of intergranular friction, σ_n is the compressive normal stress across the interface between granules, ρ_s is the solid density, and $v = dx/dt$ is the block velocity.

15

Integration of Eq. (4-6a) gives

$$v = \sqrt{\frac{2(\tau - \mu\sigma_n)x}{\rho_s B}}$$ (4-6b)

From Eqs. (4-6a) and (4-6b), the time for the granule to move across the gap bB is

$$t = B\sqrt{\frac{2\rho_s b}{\tau - \mu\sigma_n}}$$ (4-6c)

When the block moves a distance of bB, the dislocation moves a distance B. Thus, the dislocation velocity v_d is given by

$$v_d = \frac{B}{t} = \sqrt{\frac{\tau - \mu\sigma_n}{2\rho_s b}}, \quad 0 \leq v_d \leq c$$ (4-6d)

In [2], a more approximate derivation was used that produced a linear dependence on $(\tau - \mu\sigma_n)$. The new formulation Eq. (4-6d) produces weaker dependence of dislocation velocity on stress and hence lower strain rate sensitivity than the FRAGBED1 formula.

DISLOCATION NUCLEATION PROCESS

As discussed above and illustrated schematically in Figure 2, fracture of a granule has the effect of nucleating new mobile dislocations (two of opposite sign in the example of Figure 2). In an actual fragmented bed, the granules will not be equisized, but will have a distribution of sizes. We could replace the equisized blocks in Figures 1 and 2 with a commonly observed Poisson granule size distribution:

$$N_{bg}(R) = N_{bt}e^{-R/B}$$ (4-7)

16

where $N_{bg}(R)$ is the number of granules per unit volume with radii greater than R, N_{bt} is the total number of granules per unit volume, and B is thus the characteristic size of the granule size distribution.

We could then reinterpret the Bs in the previous equations as applying to the B in Eq. (4-7). However, in the results presented in this report, we have continued to assume that the granules in a computational cell all have one size, B.

The net nucleation rate of mobile dislocations can be related to the comminution rate $\partial B/\partial t$ through Eq. (4-3). Because the nucleation process does not create porosity, we can differentiate Eq. (4-3) with respect to time, and set $d\phi/dt = 0$, to obtain

$$\frac{\partial N_d}{\partial t} = -2\frac{N_d}{B}\frac{\partial B}{\partial t} \tag{4-8}$$

Substituting Eq. (4-8) into Eq. (4-4) yields

$$\frac{\partial N_d}{\partial t} = -2\frac{N_d}{B}\frac{\partial B}{\partial t} - \frac{\partial(N_d v_d)}{\partial x} \tag{4-9}$$

GRANULE COMMINUTION PROCESS

We imagine a situation like that depicted in Figure 2. Fragments, or rather the voids between them, can be thought of as dislocations gliding along planes oriented in discrete directions. Our present concern is the further fracture of the fragments, such as might occur at the potential fracture site indicated in Figure 2.

In the comminution model, fragment size, $B(\mathbf{x},t)$, decreases at a rate determined by the amount the driving stress exceeds a threshold defined by the current fragment size and the fracture toughness. At sufficiently high stresses, the rate saturates. We imagine that fragments break in two once every period Δt. Then

$$\frac{\partial B}{\partial t} = \frac{\Delta B}{\Delta t} = \frac{-\frac{1}{2}B}{\Delta t} = -\frac{1}{2}Bf \tag{4-10}$$

17

where $f = 1/\Delta t$ is the frequency of breaking. We assume that fragments contain crack-like flaws of size ηB and that linear elastic fracture mechanics applies. Fragments break if the stress intensity induced by the driving stresses exceeds the fracture toughness, i.e., if

$$\sigma_d > \left(\frac{\pi K_I^2}{4\eta B}\right)^{1/2}$$ (4-11)

The frequency is postulated to reach a limit because the cracks cannot grow faster than some speed, C_R, possibly but not necessarily the Rayleigh wave speed. The limit breaking frequency is then $C_R/2$. We ignore the possibility for crack branching. Thus, we expect the comminution rate to behave as shown in Figure 4.

We can model this behavior using

$$\frac{\partial B}{\partial t} = -\frac{1}{2}C_r S(\sigma_d, B)$$ (4-12)

where $S(\sigma_d, B)$ is a shelf function that makes a transition from 0 to 1 as the driving stress parameter σ_d increases from below the critical threshold to above the saturation limit. The threshold is determined by the current fragment size, B, and the saturation limit is chosen to be some fixed multiple of the threshold.

From an infinity of possibilities we have chosen the cumulative distribution function for the Weibull distribution [11] for our shelf function. Specifically,

$$\frac{\partial B}{\partial t} = -\frac{1}{2}C_r\left\{1 - \exp\left[-\left(\frac{\sigma_d}{\sigma_0}\right)^{\frac{e\sigma_0}{2\sigma_w}}\right]\right\}$$ (4-13)

where e is the base of the natural logarithm, the parameter σ_w specifies the half-width of the transition and the parameter σ_0 anchors the location of the transition. See Figure 4. The e arises because we normalize the Weibull shelf function so that the slope at σ_0 is $2\sigma_w/1$ (the width

divided by the rise of 1). Rather than specify the width and location of the transition directly, however, we choose to specify the threshold stress for the beginning of the transition and a parameter $m > 1$ such that the saturation stress is m times the threshold stress. The threshold depends on the current fragment size, the fracture toughness, and the relative sizes of microcracks. The threshold stress, as given by the right-hand side of Eq. (4-11), is simply the result obtained from linear elastic fracture mechanics, with any geometrical factors accounting for fragment and crack shape and orientation suppressed.

The width of the transition is defined as the difference between the threshold and saturation stresses. The location of the transition is the mean of the threshold and saturation stresses. Thus,

$$\sigma_w = (m-1)\left(\frac{\pi K_I^2}{4\eta B}\right)^{1/2} \tag{4-14}$$

and

$$\sigma_0 = \frac{1}{2}(m+1)\left(\frac{\pi K_I^2}{4\eta B}\right)^{1/2} \tag{4-15}$$

At a constant driving stress and with an initial fragment size that places the threshold below it, the comminution rate $\partial B/\partial t$ will decrease toward zero, as can be shown by substituting Eqs. (4-14) and (4-15) into the differential equation (4-13) and recasting in non-dimensional form. In effect, the rate curve in Figure 4 shifts to the right as fragment size decreases.

The comminution equation in the non-dimensional form is

$$\frac{\partial \hat{B}}{\partial \hat{t}} = -\left\{1 - \exp\left[-\left(\hat{B}^{\frac{e[m+1]}{8[m-1]}}\right)\right]\right\} \tag{4-16}$$

where

$$\hat{B} = \frac{16\eta\sigma_d^2}{\pi K_I^2(m+1)^2}B \tag{4-17}$$

19
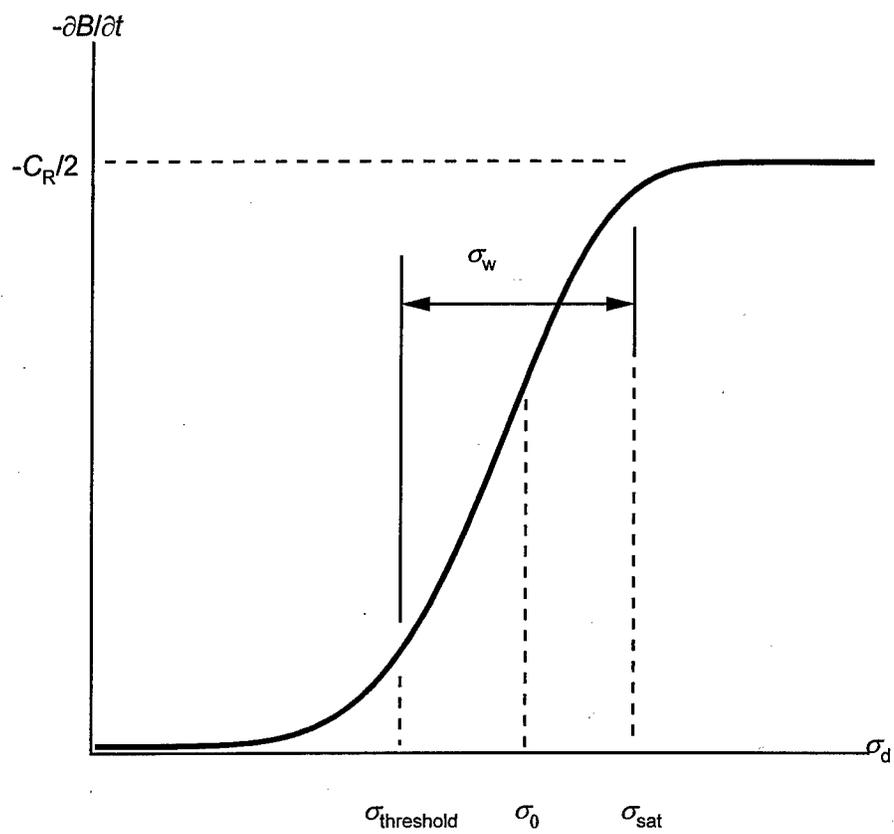
Figure 4. Comminution rate as a function of driving stress.

and

$$\hat{t} = \frac{8C_r\eta\sigma_d^2}{\pi K_I^2(m+1)^2}t \tag{4-18}$$

As $\hat{B}$ approaches zero from above, $\partial\hat{B}/\partial\hat{t}$ approaches zero, and comminution ceases. For the parameter values in Table 1,

$$\hat{B}(0) = 1.10\times10^5\,\mathrm{m^{-1}}B(0) \tag{4-19}$$

and

$$\hat{t} = 2.75\times10^8\,\mathrm{s^{-1}}t \tag{4-20}$$

i.e., for an initial fragment size around 10 μm, the non-dimensional initial size is around 1, and for a duration of 1 μs, the non-dimensional duration is around 275.

Table 1

COMMINUTION MODEL PARAMETERS

Parameter	Symbol	Value
Relative crack size	η	0.1
Maximum crack speed	C_R	5000 m/s
Driving stress	σ_d	4 GPa
Fracture toughness	K_I	$4\,MPa\sqrt{m}$
Saturation stress multiplier	m	1.15

We can exercise the FRAGBED2 comminution equations independently by considering the compression and shearing of a thin layer of ceramic that is infinite in extent. If we assume that stresses are homogeneous and equilibrated (i.e., that the layer is thin, then the comminution equation (4-16) is a set of ordinary differential equations in time, one equation per slip plane. In

21

general, the comminution law differential equation (4-16) cannot be integrated analytically, but we can solve numerically for fixed stress using *Mathematica* software [12].

Several numerical solutions and their exponential decay approximations are compared in Figure 5 for a small matrix of the parameters $\hat{B}(0)$ shown in Table 2. We performed L2D hydrocode [13] calculations using a single element to check our implementation of the comminution model. The *Mathematica* numerical solution and the L2D solution are virtually identical.

Table 2

MATRIX OF COMMINUTION MODEL PARAMETER VARIATIONS

$m \downarrow \quad \hat{B}(0) \rightarrow$	0.5	1.0	1.5
1.05	X	X	X
1.10	X	X	X
1.15	X	X	X

For very large times, the solution to the comminution equations under constant stress loading approaches a power law decay, independent of $\hat{B}(0)$:

$$\hat{B}(\hat{t}) \propto \hat{t}^{\frac{8(m-1)}{8(m-1)-e(m+1)}} \tag{4-21}$$

where e is the base of the natural logarithm. For certain values of $\hat{B}(0)$, the solution follows a power law decay for all times. For other values of $\hat{B}(0)$, the solutions approach power law decay more slowly for larger values of m.

LOCAL STRESSES

Local stress variations around the average or continuum stress state occur within a RVE, and these local stresses are important in the comminution process. Following an approach by Costin [14], local stresses are calculated on each plane that are different from the average or continuum stresses. These local stresses are meant to reflect the existence within the RVE of

22
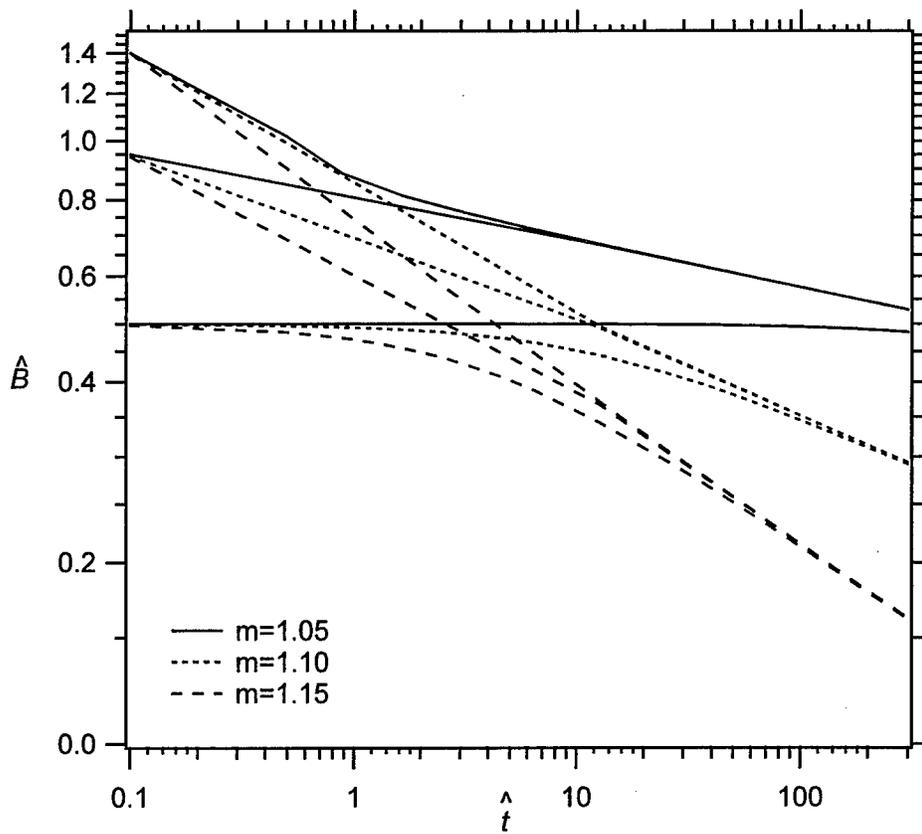
Figure 5. Normalized fragment size as a function of normalized time.

local stress variations around the average due to granule interactions. The local stresses are used to govern the comminution within a RVE, but are not used to transfer momentum to adjacent meshes. (The average stresses are used in the equations for conservation of mass and energy.)

In the comminution equations, we therefore allow σ_d to be a local stress defined by

$$\sigma_d^2 = m_1 \tau^2 + m_2 \sigma_n^2 \tag{4-22}$$

where the *m*'s are adjustable parameters.

SECTION 5

NUMERICAL IMPLEMENTATION IN HYDROCODES

SOLUTION PROCEDURE FOR SLIP PLANE EQUATIONS

We follow the work by Peirce et al. [15] on slip in single crystals. We decompose the total deformation tensor

$$\mathbf{F} = \mathbf{F}_e \mathbf{F}_p \qquad (5\text{-}1)$$

into an elastic deformation tensor and a plastic deformation tensor. Given the plastic deformation $\mathbf{F}_p$, we can solve for the elastic deformation $\mathbf{F}_e$ from Peirce's Eq. (18). The total deformation $\mathbf{F}$ is input into the FRAGBED routine. Because as the elastic constitutive equation is assumed to be isotropic, we can make Cauchy stress a direct function of $\mathbf{V}_e$ (see Malvern [16], Eq. 6.8.35), where $\mathbf{V}_e$ is defined from the left polar decomposition of $\mathbf{F}_e$:

$$\mathbf{F}_e = \mathbf{V}_e \mathbf{R}_e \qquad (5\text{-}2)$$

and where $\mathbf{R}_e$ is the elastic rotation tensor (see [16], Eq. 4.6.1). We use logarithmic strain

$$\hat{\varepsilon} = Ln(V_e) \qquad (5\text{-}3)$$

where **Ln** stands for the tensor logarithm of a tensor. Finally, we have the evolution equation for the plastic deformation tensor:

$$\frac{d\mathbf{F}_p}{dt} = \sum_k \left[\dot{\gamma}_p^k \left(\mathbf{s}^k \otimes \mathbf{n}^k \right) \right] \mathbf{F}_p \qquad (5\text{-}4)$$

25

Here, $\dot{\gamma}_p^k$ is the non-elastic shear strain rate on the k th slip plane, and $\mathbf{s}^k$ and $\mathbf{n}^k$ are the slip direction and slip plane normal unit vectors, respectively. The symbol $\otimes$ denotes the dyadic product. Henceforth, we will suppress the superscript k but assume that it is there.

Vectors $\mathbf{s}$ and $\mathbf{n}$ are referred to as the plastic configuration (determined by $\mathbf{F}_p$), and $\mathbf{s}^*$ and $\mathbf{n}^*$ are the corresponding vectors in the current configuration (determined by $\mathbf{F}$).

$$\mathbf{n}^* = \mathbf{n}\mathbf{F}_e^{-1} \tag{5-5a}$$

The slip plane normal $\mathbf{n}$ is simply a constant vector given by the original orientation of the plane. The assumption is that only elastic deformations change the orientation of a plane. The slip direction $\mathbf{s}^*$ is given by the following equations

$$\mathbf{t} = \mathbf{n}^*\boldsymbol{\sigma} \tag{5-5b}$$

$$\sigma_n = \mathbf{n}^* \cdot \mathbf{t} \tag{5-5c}$$

$$\mathbf{s}^* = \mathbf{t} - \sigma_n \mathbf{n}^* \tag{5-5d}$$

$$\mathbf{s} = \mathbf{F}_e^{-1}\mathbf{s}^* \tag{5-5e}$$

Here, $\boldsymbol{\sigma}$ is the stress tensor, $\mathbf{t}$ is the traction vector on the plane and σ_n is the normal stress on the plane. Equations (5-5c,d) ensure that vectors $\mathbf{s}^*$ and $\mathbf{n}^*$ are orthogonal. From Eq. (5-5a,e) it follows that $\mathbf{s}$ and $\mathbf{n}$ are orthogonal whenever $\mathbf{s}^*$ and $\mathbf{n}^*$ are orthogonal. Equation (5-5e) follows from the definition of a deformation tensor. Equation (5-5a) does not have a similar physical meaning, but is simply a formula that generates a vector that is normal to any vector that lies in the slip plane. The various vectors $\mathbf{s}, \mathbf{s}^*, \mathbf{n},$ and $\mathbf{n}^*$ must be normalized before use in equations like (5-4).

Analytically, the plastic deformation tensor will always be incompressible for the following reason. The plastic strain rate tensor on each individual plane, $\dot{\gamma}_p^k \mathbf{s}^k \otimes \mathbf{n}^k$, is traceless because the tensor product between two vectors that are normal to each other is traceless. The

sum of a set of traceless tensors is also traceless. Equation (5-4) has the same form as the rate of the total deformation tensor, see [16], Eq. 4.5.14:

$$\frac{d\mathbf{F}}{dt} = \mathbf{LF} \tag{5-6}$$

where $\mathbf{F}$ is the deformation tensor and $\mathbf{L}$ is the velocity gradient. Whether we choose to interpret the sum of the tensors $\gamma_p^k \mathbf{s}^k \otimes \mathbf{n}^k$ as a plastic velocity gradient, $\mathbf{L}_p$, or not, mathematically the rate of the plastic deformation tensor has the same form as the rate of the total deformation tensor. Therefore, because a traceless $\mathbf{L}$ (zero volumetric strain rate) leads to incompressible flow, a traceless $\mathbf{L}_p$ will lead to incompressible plastic flow.

Numerically there is potentially a problem with incompressibility. We use the following finite difference equation to update $\mathbf{F}_p$:

$$\frac{\left(\mathbf{F}_p^{n+1} - \mathbf{F}_p^n\right)}{\Delta t} = \frac{1}{2}\mathbf{L}_p\left(\mathbf{F}_p^{n+1} + \mathbf{F}_p^n\right) \tag{5-7a}$$

Superscript n stands for time step level. The rhs is correctly time centered at $n+1/2$ because $\mathbf{L}_p$ is ordinarily centered on half time steps. Rearranging we get

$$\left(1 - \frac{\Delta t}{2}\mathbf{L}_p\right)\mathbf{F}_p^{n+1} = \left(1 + \frac{\Delta t}{2}\mathbf{L}_p\right)\mathbf{F}_p^n \tag{5-7b}$$

The equation can be solved as a linear equation system for the unknown $\mathbf{F}_p^{n+1}$ using Cramer's rule. Therefore, we again rearrange

$$\mathbf{F}_p^{n+1} = \left(1 - \frac{\Delta t}{2}\mathbf{L}_p\right)^{-1}\left(1 + \frac{\Delta t}{2}\mathbf{L}_p\right)\mathbf{F}_p^n \tag{5-7c}$$

Everything on the rhs is known. In principle, the fact that the determinant of $\left[1-(\Delta t/2)\mathbf{L}_p\right]$ must be non-zero poses a restriction on Δt. In practice, a zero determinant means that the flow is so quick that the cell inverts in a single time step. In that case, the calculations would abort before applying the above equations.

When we test Eq. (5-7c) above, we find that incompressibility is satisfied to within machine roundoff. We do not yet completely understand how this fortuitous situation comes about, but the correct time centering of the rhs of Eq. (5-7a) may be critical.

The plastic flow is modeled entirely as slip on discrete slip planes. We have equilibrium on a certain plane when

$$\tau \le c + \mu\sigma_n \tag{5-8a}$$

where c is the cohesion, while we will get slip when

$$\tau > c + \mu\sigma_n \tag{5-8b}$$

When we have slip on one or several planes, the plastic deformation tensor has to be modified to reduce the resolved shear stresses. Because the dislocations have a limited mobility, the reduction in the resolved shear stress is subject to a limit on the plastic strain rate.

$$\dot{\gamma}_p \le gbBN_dv_d \tag{5-9}$$

where g is a proportionality factor, b is the burgerís vector, B is the block size, N_d is the dislocation density, and v_d is the dislocation velocity. An initial thought is to enforce

$$\tau = c + \mu\sigma_n \tag{5-10}$$

on all planes that want to slip.

28

The following example with a pair of slip planes at right angles shows why this approach does not generally work. One plane is along the x axis, the other plane along the y axis. We assume 2D symmetry, which means that the direction of the resolved shear stress is in the x-y plane. On the plane with the normal in the y direction, Eq. (5-10) requires

$$\tau_{yx} = c + \mu\sigma_{yy} \qquad (5\text{-}11a)$$

while on the plane with the normal in the x direction, Eq. (5-10) requires

$$\tau_{xy} = c + \mu\sigma_{xx} \qquad (5\text{-}11b)$$

The symmetry of the stress tensor requires $\tau_{yx} = \tau_{xy}$, while at the same time σ_{xx} will not generally be equal to σ_{yy}. This example shows that we cannot generally expect to fulfill Eq. (5-10) on several slip planes at the same time.

We therefore implemented a scheme where we solve one plane at a time. The plane with largest plastic strain rate is processed first. The processing order is important because a change in shear stress on one plane may change the stress state on some other plane. We must also check at the next plane to be processed to see if the no slip condition, Eq. (5-8a), has been fulfilled. If not, we back-calculate a trial strain rate from

$$\dot{\gamma}_p = \frac{(\tau - \mu\sigma_n)}{G\Delta t} \qquad (5\text{-}12)$$

where G is the shear modulus. This equation gives the strain rate that relieves the overshear in a single time step. This strain rate is limited by Eq. (5-9). The shear modulus enters as one G because we are slipping on one plane. The cohesion does not appear in Eq. (5-12) because it is set to zero after the first slip. We have found that the cohesion makes little difference to the results, so we have not implemented anything more elaborate.

Equation (5-12) assumes an infinitesimal linear Hooke's law. Because of constitutive and geometric non-linearities we have to iterate while fine adjusting $\dot{\gamma}_p$. The ultimate goal is

$$\tau - \mu\sigma_n = 0 \tag{5-13}$$

All this is subject to the limit on the strain rate from Eq. (5-9).

The model assumes that there is a porosity ϕ_s associated with each slip plane, given by

$$\phi_s = 1.5N_d bB^2 \tag{5-14a}$$

The total porosity ϕ is given by the linear sum of Eq. (5-14) over all the slip planes.

In the present formulation the porosity affects the pressure equation of state. We are using a Mie-Grüneisen $P(V, E)$ relation. The specific volume V that enters the equation of state is modified to

$$V = (1 - \phi)V_g \tag{5-15b}$$

where V_g is the macroscopic specific volume. At zero porosity the macroscopic and equation of state volumes are the same. As the porosity increases for a constant macroscopic volume the pressure increases, too.

WELL-POSEDNESS, THERMODYNAMIC RESPECTABILITY, MESH SIZE INDEPENDENCE, AND INTERNAL CONSISTENCY REQUIREMENTS

FRAGBED2, a mesomechanical internal state variable model, is similar to the type discussed by Coleman and Gurtin [17], who provided a recipe that guarantees well-posedness and thermodynamic respectability. However, FRAGBED2 does not exactly fit the Coleman and Gurtin recipe for internal state variable models because it contains a flux term in the evolution equation for the mobile dislocation density N_d. However, we can use an approach developed by Whitham [18, 19] to analyze the shear wave propagation equation across each slip plane, and thereby establish well-posedness and thermodynamic respectability.

Consider one of the slip planes in FRAGBED2. If we define the slip to be in the x direction, and the normal to the slip plane to be the y direction, and x and y are Lagrangian

coordinates, then the conservation of momentum and the mass equations on that slip plane become:

Momentum:
$$\rho \frac{\partial u}{\partial t} = \frac{\partial \tau}{\partial y}$$
(5-16)

Mass:
$$\frac{\partial \gamma}{\partial t} = \frac{\partial u}{\partial y}$$
(5-17)

where u is the particle velocity in the x direction, ρ is the density, τ is the shear stress across the slip plane, and γ is the strain (displacement gradient) associated with the slip.

The constitutive relation for slip on the plane is

$$\frac{\partial \gamma}{\partial t} = \frac{1}{G} \frac{\partial \tau}{\partial t} + b N_d B v_d(\tau)$$
(5-18)

where G is the shear modulus, b is the relative macrodislocation size (dimensionless), $\mathbf{B}$ is the granule size, N_d is the mobile macrodislocation density (number per unit area), and v_d is the stress-dependent macrodislocation velocity. The first term on the rhs. of Eq. (5-18) is the elastic strain rate, and the second term is the plastic strain rate due to granular slip on the slip plane.

Next we operate on Eq. (5-16) with $\partial/\partial y$ and on Eq. (5-17) with $\partial/\partial t$, and combine with Eq. (5-18) to obtain:

$$\frac{1}{\rho} \frac{\partial^2 \tau}{\partial y^2} = \frac{1}{G} \frac{\partial^2 \tau}{\partial t^2} + \frac{\partial(N_d b B v_d)}{\partial t}$$
(5-19)

The FRAGBED 2 comminution and dislocation nucleation models yield

$$\frac{1}{N_d} \frac{\partial N_d}{\partial t} = -\frac{2}{B} \frac{\partial B}{\partial t} - \frac{1}{N_d} \frac{\partial(N_d v_d)}{\partial x}$$
(5-20)

31

Combining Eqs. (5-19) and (5-20) yields

$$\frac{\partial^2 \tau}{\partial t^2} - \frac{G}{\rho}\frac{\partial^2 \tau}{\partial y^2} + \lambda\frac{\partial \tau}{\partial t} + F = 0 \tag{5-21}$$

where $\lambda = bBGN_d\,\partial v_d/\partial \tau$

and

$$F = bBGN_d v_d\left[-\frac{1}{B}\frac{\partial B}{\partial dt} - \frac{1}{N_d}\frac{\partial(N_d v_d)}{\partial x}\right] \tag{5-22}$$

We first note that λ is always positive, because b, B, G, N_d, and $\partial v_d/\partial \tau$ are positive. The reason that $\partial v_d/\partial \tau$ is positive is that the model requires higher shear stresses to increase the dislocation velocity, i.e., the system is dissipative.

The FRAGBED 2 comminution model makes $\partial B/\partial t$ a function of the stresses. Thus F is a function of the stresses, N_d, and the macrodislocation flux in the x direction, $\partial(N_d V_d)/\partial x$.

We next linearize Eq. (5-21) by holding all the variables constant at their values at a given instant (labeled by the subscript 0) and then replacing τ by $\tau_0 + \Delta$. Then Eq. (5-21) becomes

$$\frac{\partial^2 \Delta}{\partial t^2} - \frac{G}{\rho}\frac{\partial^2 \Delta}{\partial y^2} + \lambda_0\frac{\partial \Delta}{\partial t} + F_0 = 0 \tag{5-23}$$

Next we define
$$D = \Delta + \frac{F_0 t}{\lambda_0} \tag{5-24}$$

Combining Eqs. (5-23) and (5-24) yields

$$\frac{\partial^2 D}{\partial t^2} - \frac{G}{\rho}\frac{\partial^2 D}{\partial y^2} + \lambda_0 \frac{\partial D}{\partial t} = 0 \qquad (5\text{-}25)$$

Eq. (5-25) is of the form shown by Whitham to have solutions that are both unique and stable. Stability means that D decreases with time. Taking the time derivatives of Eq. (5-24) yields:

$$\frac{\partial D}{\partial t} = \frac{\partial \Delta}{\partial t} + \frac{F_0}{\lambda_0} < 0 \qquad (5\text{-}26)$$

F_0 can be positive or negative, depending on the comminution rate and macrodislocation flux. If the comminution rate is zero, for example, F_0 will be negative if the macrodislocation density is decreasing because more macrodislocations are flowing out of the mesomechanical relevant volume element (RVE) than into it. In any event, if F_0 is positive, $\partial \Delta / \partial t$ will be negative, and must be greater in absolute magnitude than F_0 / λ_0. However, if F_0 is negative, $\partial \Delta / \partial t$ can be positive, but must have an absolute value less than that of F_0 / λ_0.

In summary, the FRAGBED 2 model should satisfy well-posedness and thermodynamic respectability requirements because the shear wave equations associated with each slip plane satisfy Whitham's criteria. Because the same analysis applies to each slip plane, the uniqueness and stability requirements should also be satisfied for an RVE containing many such planes. The physical reason for thermodynamic respectability is that the granule comminution and flow process is dissipative.

Internal consistency is defined as the requirement that the mesomechanical model does not predict large variations in calculated variables over the dimension of the RVE. Compliance with both this requirement and that of mesh size insensitivity must be demonstrated for each specific application.

SECTION 6

EXPERIMENTS FOR CALIBRATION AND VALIDATION OF FRAGBED2

CAVITY EXPANSION EXPERIMENTS

Calibration of the comminution parameters in FRAGBED2 requires an experiment that applies a known, relevant stress and strain history to a specimen, then allows the specimen to be recovered to quantify and correlate the damage. Impact recovery experiments in which a thin stelliform flyer impacts a ceramic specimen to produce a single well-characterized stress pulse would be useful for calibrating the comminution model. Such experiments have been performed on aluminas similar to our AD-995 [20], but only at stress levels insufficient to cause significant comminution.

In work reported elsewhere [21, 22], experiments were performed by detonating an explosive charge within a spherical cavity machined in a ceramic specimen confined in an impedance-matching bronze container. The resulting loading of the material (stress, strain, and strain rate) is well characterized, nominally one-dimensional, and is similar to the conditions occurring near the tip of a rod projectile during a penetration event. The test is instrumented with electromagnetic particle velocity history gages located at several radii from the charge. Posttest microscopic examination of the recovered samples has revealed an overall damage less severe than in typical penetration experiments, and has allowed a more detailed description of the fracture and comminution processes.

The spherical cavity expansion experiments [21,22] provide an order-of-magnitude estimate of fragment size as a function of time and stress level. In experiments on AD-995, stresses near the cavity wall were estimated to be around 8 GPa, pulse durations were on the order of 1 μs, and fragment sizes were on the order of 10 μm. Corresponding normalized values are $\hat{t} = 275$, and $\hat{B} = 1$. Comparing these values with the results shown in Figure 5, we see that $\hat{B} = 1$ at $\hat{t}=275$ corresponds to a value of m greater than 1.15.

The FRAGBED2 model in L2D does a reasonably good job of matching particle velocity histories measured in spherical cavity expansion tests on Coors AD-995 alumina (see Figure 6).
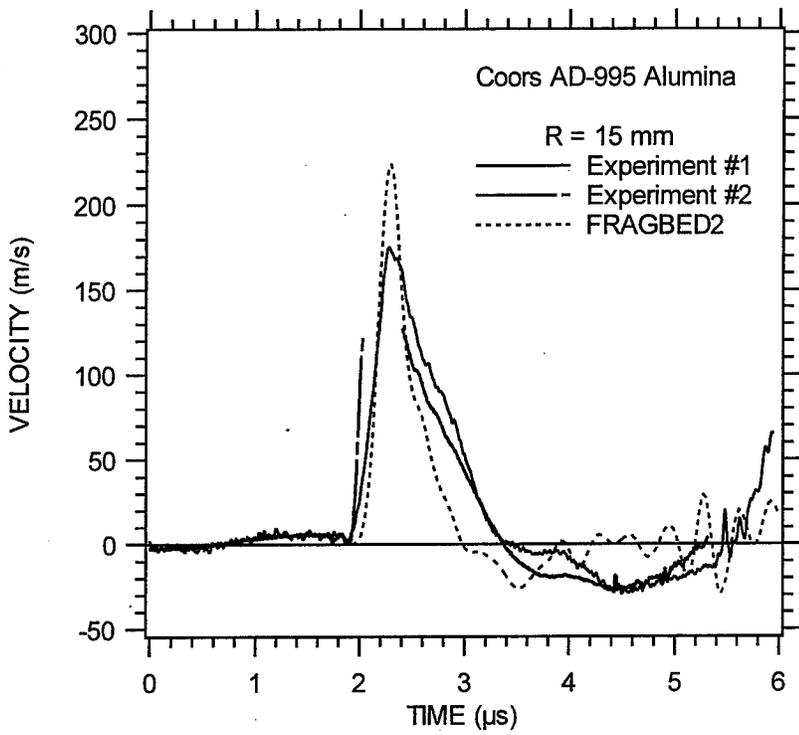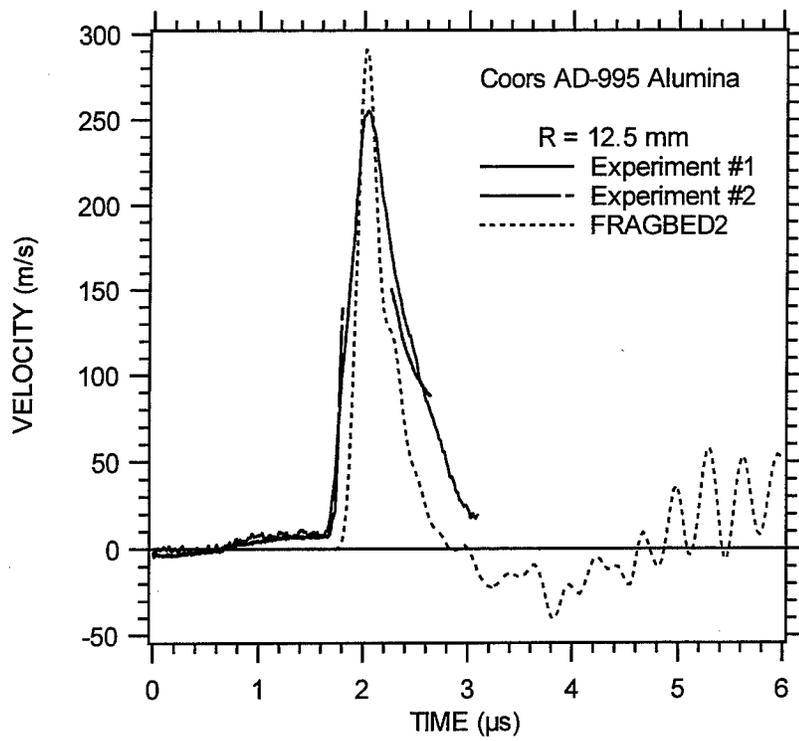
Figure 6. Comparison of measured radial particle velocity at different radii with those computed by FRAGBED2 in L2D. (continued)
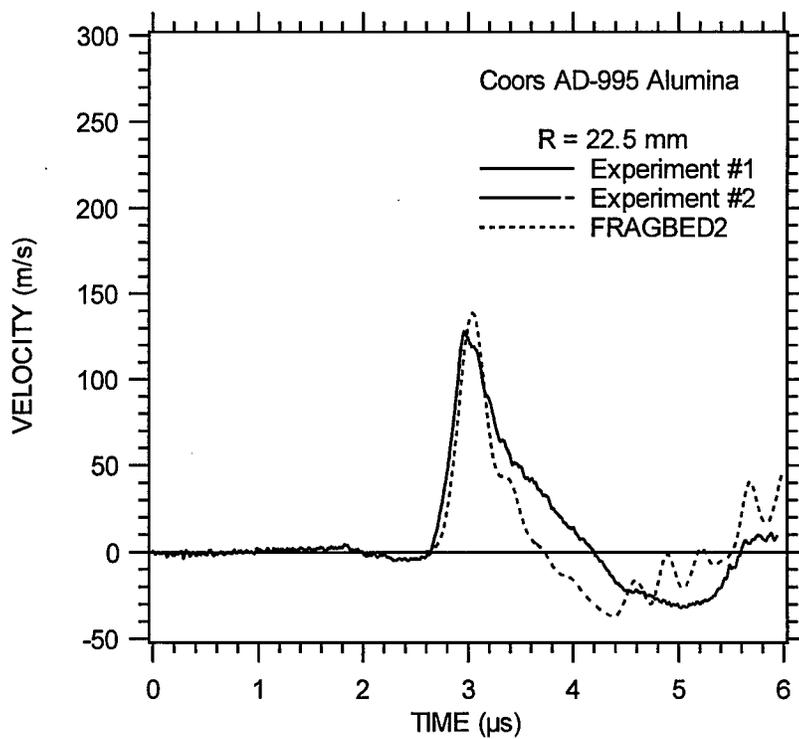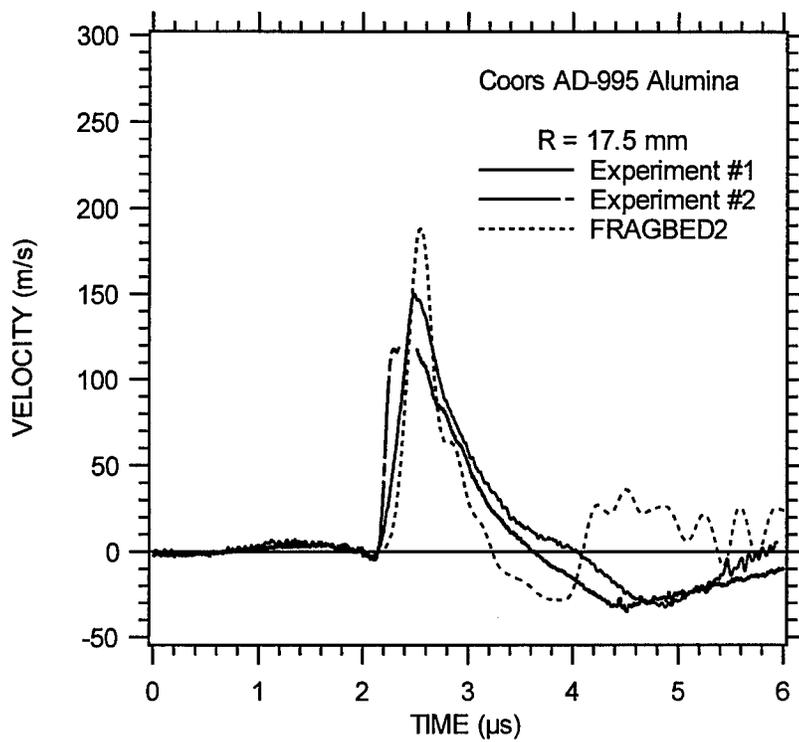
36

Figure 6. Comparison of measured radial particle velocity at different radii
with those computed by FRAGBED2 in L2D. (concluded)

37

The results are sensitive to the initial fragment size distribution B_0 computed using Eq. 3-6. We found that the results were also sensitive to the choice of limiting crack speed (or breaking frequency), C_R (see Eq. 4-13). C_R is essentially a parameter that scales time. We found that if B_0 was too small or C_R too large, comminution proceeded too quickly, the response was too non-elastic, and the velocity waveforms did not display the negative rebound phases that are in the measured histories. By our choice of m, B_0, and C_R, we could compute final fragment sizes that matched the experiments. In particular, the variable-size initial fragment bed approach outlined in Eq. 3-1 to 3-6 was used, with $K_c = 4\,\mathrm{MPa}\sqrt{\mathrm{m}}$, $P_0 = 15.5\,\mathrm{GPa}$, and $a = 0.01$ m. Those parameter values, along with a uniform initial porosity, $\phi_0 = 5.85\times10^{-6}$, $m = 1.5$, and $C_R = 496$ m/s (see Eq. 4-10 through 4-15), gave the result that nearly all of the comminution occurred within about a millimeter of the charge, as was observed in the experiments. In the thin comminuted zone, the porosity rose rapidly to 3% within 6 µs, by the influx of dislocations from the wall of the spherical cavity. Experiments with stronger charges and therefore greater comminution would be useful for calibrating the comminution model.

INVESTIGATION OF SHEAR LOCALIZATION IN CERAMICS USING A MODIFIED THICK-WALLED CYLINDER METHOD

Note: The thick-walled cylinder experiments were designed with the help of Professor Vitali F. Nesterenko, University of California, San Diego. He will be a co-author of the journal manuscript resulting from the following section.

Compared to steels, ceramic armors are attractive from the standpoint of weight. To design ceramic armors efficiently, good computational models are needed that include the relevant material physics. Shockey et al. [1] describe the relevant physics to include the fracture of the ceramic, the comminution of the fractured ceramic into a fragmented bed (the Mescall zone), and the subsequent flow of the fragmented bed out of the penetrator's path. Curran et al. developed a computational model, FRAGBED [2,21], that captures these physics. Other models have also been developed for ceramic behavior under armor penetration conditions [23-25]. To calibrate any of these models, tests are required that exercise the relevant physics in relative isolation. In particular, a test is needed that subjects ceramic to intense, high rate, compressive flows like those in the Mescall zone, which is the zone immediately in front of an advancing penetrator. Nesterenko et al. developed the thick-walled cylinder method (TWCM) [26,27] to meet these requirements.

Nesterenko et al. applied the TWCM to study the large deformation, high strain rate behavior of metals [28], reactive mixtures [29], ceramic powders [30], and intact ceramics [31]. In the TWCM, depicted schematically in Figure 7, a copper tube is inserted inside a thick-walled tube of specimen material. This assembly is in turn inserted inside a copper outer tube. The outer tube is surrounded by explosive which, when detonated, compresses the assembly radially inward. By sectioning the recovered assembly and measuring the radial displacement, the circumferential strain in the ceramic can be quantified and the amount of fragmentation and shear banding related to the strain. The TWCM is attractive because it allows specimens to be subjected to intense rapid loading yet be recovered.

In the original application of the TWCM to ceramics [30,31], the tube assembly was subjected to two explosions. For the first explosion, a solid copper rod rather than a tube was inserted in the inner bore of the specimen. The first explosion fragmented and compacted the specimen into an in situ fragment bed but did not strain it much. Before the second explosion, the solid copper rod was drilled out to form a tube. The second explosion compressed the assembly inward until the drilled hole collapsed completely. The amount of strain was controlled by varying the diameter of the drilled hole. Clearly, the need for two explosions complicates the TWCM when applied to ceramics.

We realized, however, that the need for two explosions can be eliminated. As shown in Figure 8, by tapering the bore of the inner copper tube or by inserting a tapered pin into a straight bore, the diameter of the bore (and therefore the allowed range of strain) can be varied along the length of the assembly from near zero at the solid end to as much as needed at the open end. The tapered pin scheme was chosen for implementation because of the difficulty associated with machining a tapered bore.

In this section of the report, we (1) describe the tapered TWCM, (2) show its application to alumina ceramic to illustrate high rate flow phenomenology and the transition to localized deformation, and (3) present data for validating the FRAGBED2 ceramic comminution and fragment flow model. Details of the tapered TWCM are presented so that others can model the experiment. Results for Coors AD-998 alumina are shown. Among the results, particular emphasis is placed on shear band phenomenology and implications for the fragment flow picture of ceramic deformation. Also included are the results of simulating the experiment using a two-dimensional hydrocode.
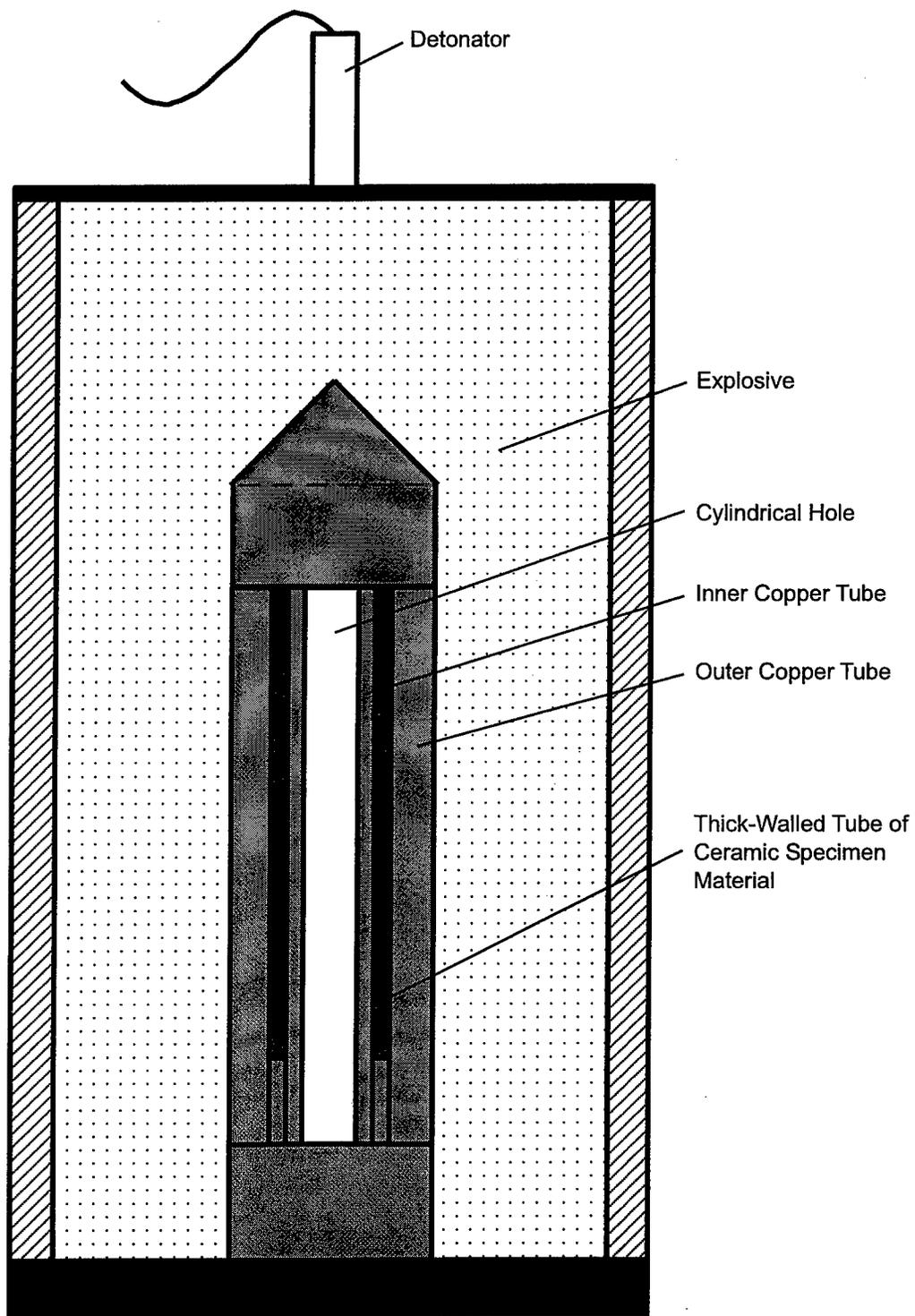
Figure 7. Original Nesterenko thick-walled cylinder method.

Detonator

Foam Attenuator

Explosive

Tapered Brass Pin

Inner Copper Tube

Outer Copper Tube

Thick-Walled Tube of
Ceramic Specimen
Material
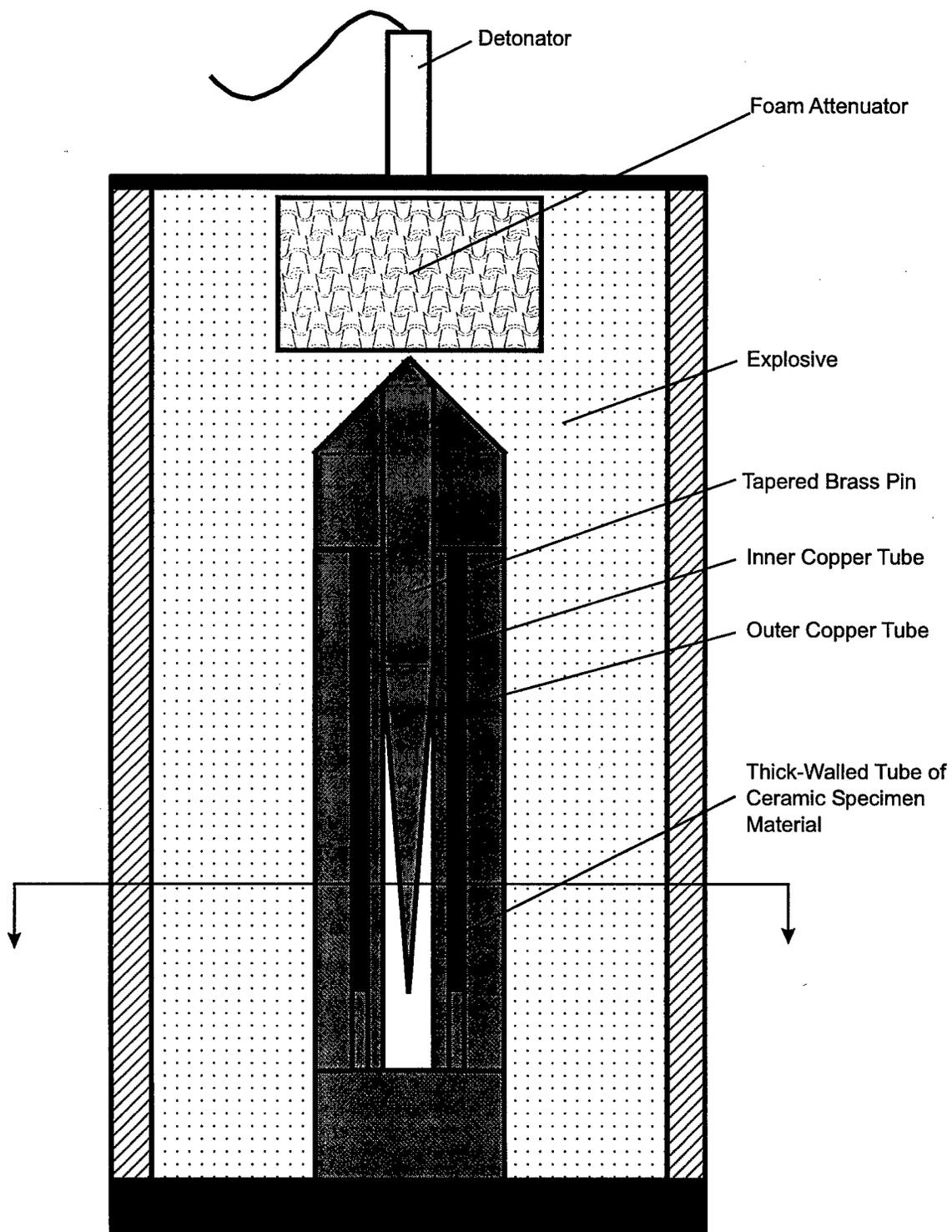
Figure 8. Modified thick-walled cylinder method. (Continued)

41
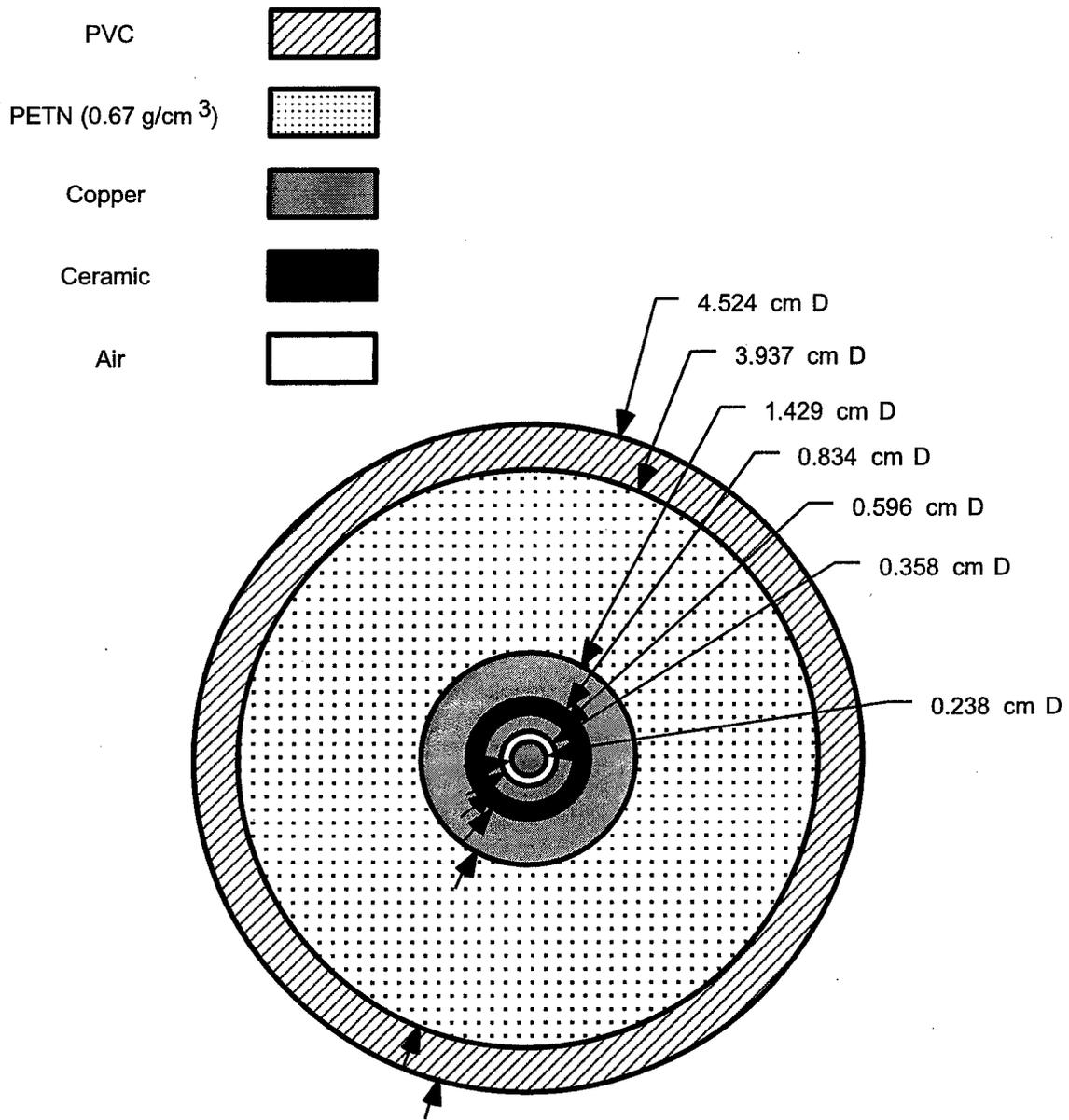
Figure 8. Modified thick-walled cylinder method. (Concluded)

Extruded AD-998 alumina ceramic tubes 11.1-mm outside diameter, 7.9-mm inside diameter, and 44.5-mm long were obtained from Coors Ceramics, Golden, CO. The alumina was reported to be 99.8% pure with porosity around 1%. The porosity is estimated from the ratio of the theoretical density of α-alumina, 3.97 g/cm^3, to that of extruded AD-998, 3.92 g/cm^3. As depicted in Figure 8, the tubes were fitted into and onto copper tubes with about 50 μm of clearance. The assemblies were completed by inserting copper rings below the specimens and inserting the brass pin through the conical cap and into the inner tube. Finally, the momentum trap was bonded to the bottom of the assembly and the brass pin was bonded to the cap with cyanoacrylate adhesive. The assembly was then placed inside a 100-mm length of PVC pipe and topped with a foam attenuator. About 130 g of PETN explosive was packed around the assembly and covered with a disk of sheet explosive. The explosion was initiated from the center of the disk. The recovered assemblies were sectioned, polished, and micrographed.

Transverse optical photographs of sections at 10-mm intervals measured from the most deformed end of the ceramic are shown in Figure 9, and a longitudinal section is shown in Figure 10. Average radial displacements, u, finite Lagrangian hoop strains, $\varepsilon_{\theta\theta}$, and radial strains, ε_{rr}, are computed for each section from the radial displacement, u_0, of the inner wall of the inner copper tube from its initial position, $R_0 = 2.38$ mm, to its final position against the tapered pin, assuming incompressible, plane deformation.

$$u = R - \sqrt{R^2 - 2R_0 u_0 + u_0^2} \tag{6-1}$$

$$\varepsilon_{rr} = \frac{1}{2}\left(\frac{R^2}{R^2 - 2R_0 u_0 + u_0^2} - 1\right) \tag{6-2}$$

$$\varepsilon_{\theta\theta} = \frac{1}{2}\left[\frac{u_0(u_0 - 2R_0)}{R^2}\right] \tag{6-3}$$

The strains are plotted in Figure 11.

As revealed in the Figure 9 cross sections, a significant portion of the total deformation is accommodated by displacement jumps across shear bands. Figure 12 shows that if all the deformation were accommodated in one logarithmic spiral shear band, then an approximate

43
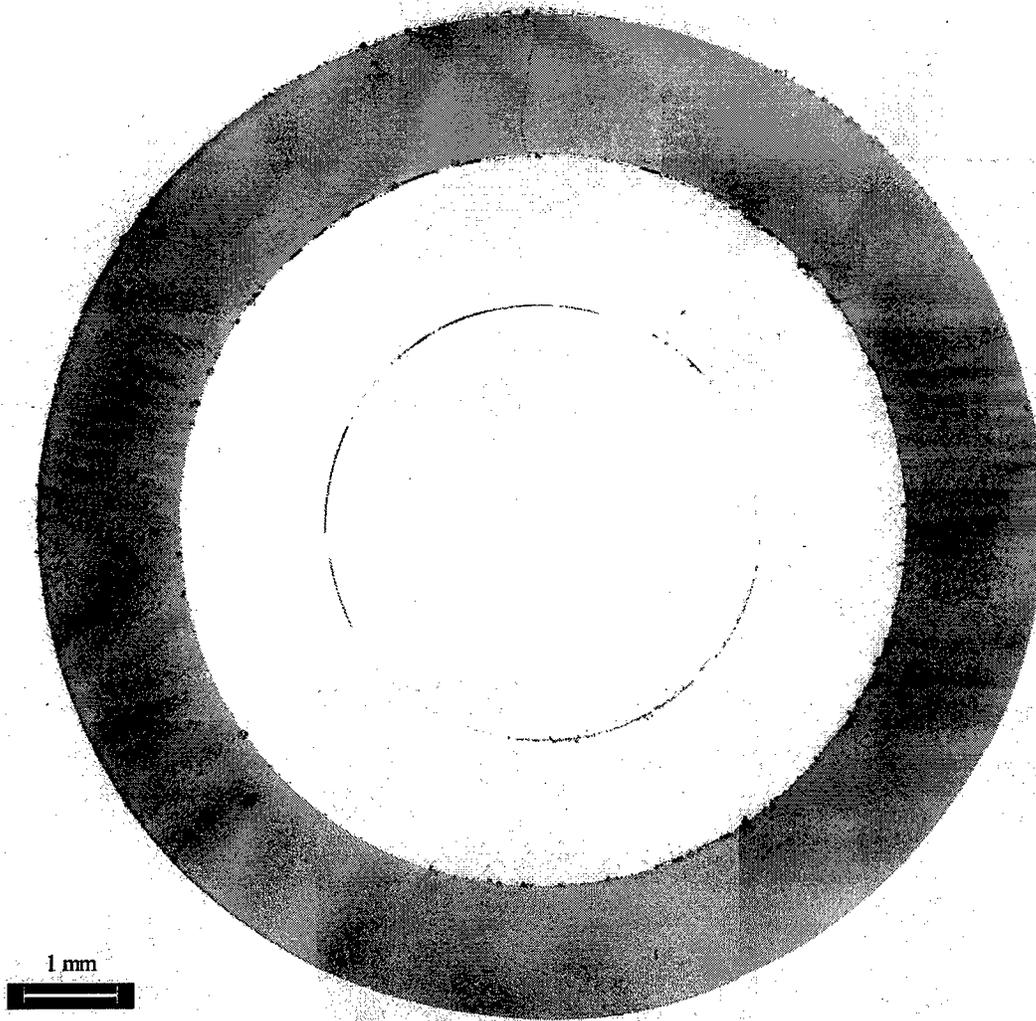
$$\varepsilon_{\theta\theta} \approx 0$$

(a)

Figure 9. TWCM cross sections from different locations along the taper, with average hoop strains shown. (continued)

1 mm
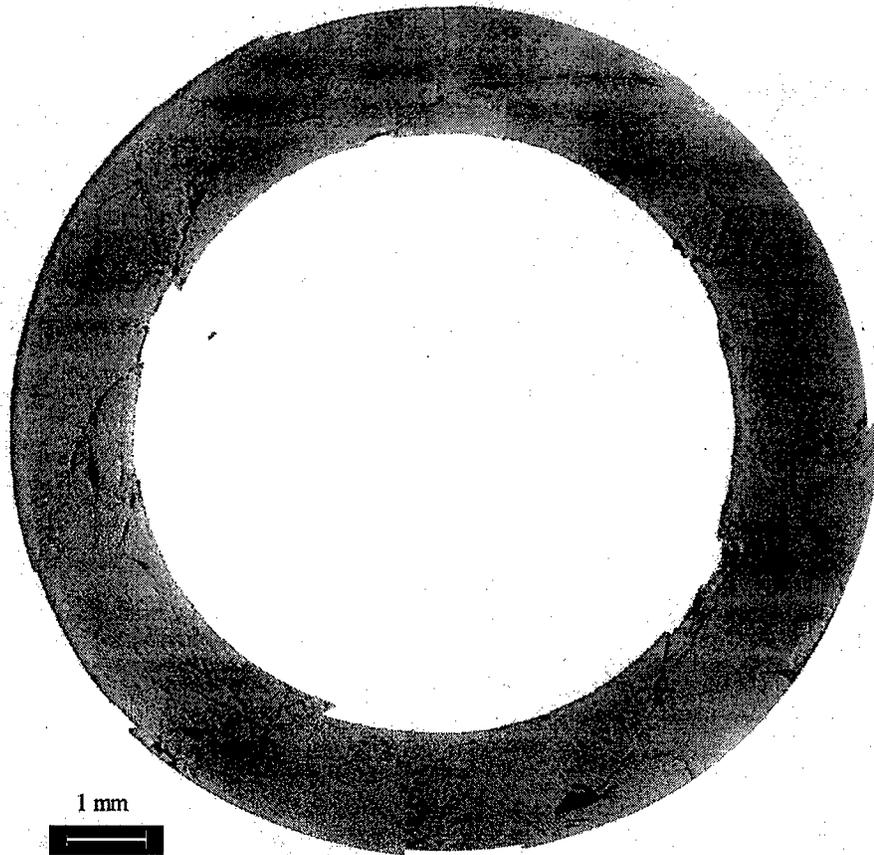
$\varepsilon_{66} \approx -0.04$

(b)

Figure 9. TWCM cross sections from different locations along the taper, with average
hoop strains shown. (continued)
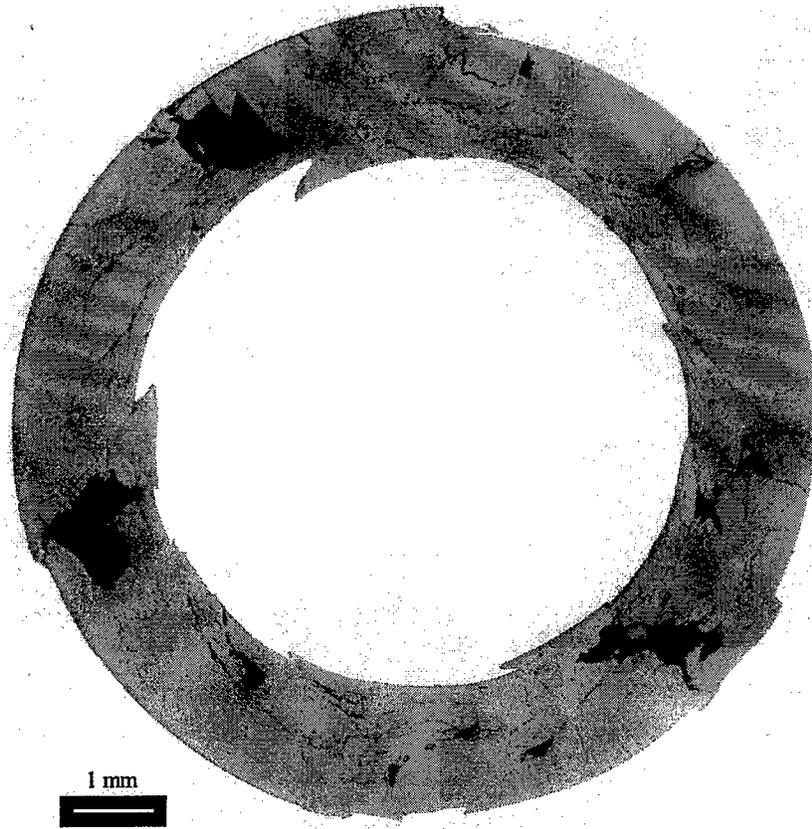
$$\varepsilon_{\theta\theta} \approx -0.09$$

(c)

Figure 9. TWCM cross sections from different locations along the taper, with average hoop strains shown. (continued)
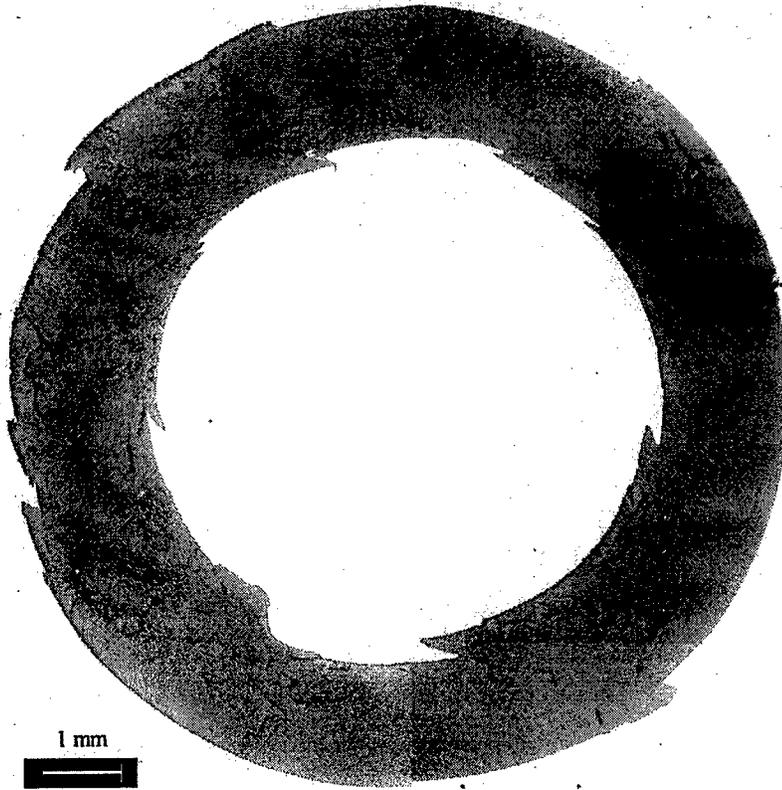
$$\varepsilon_{\theta\theta} \approx -0.12$$

(d)

Figure 9. TWCM cross sections from different locations along the taper, with average
hoop strains shown. (concluded)
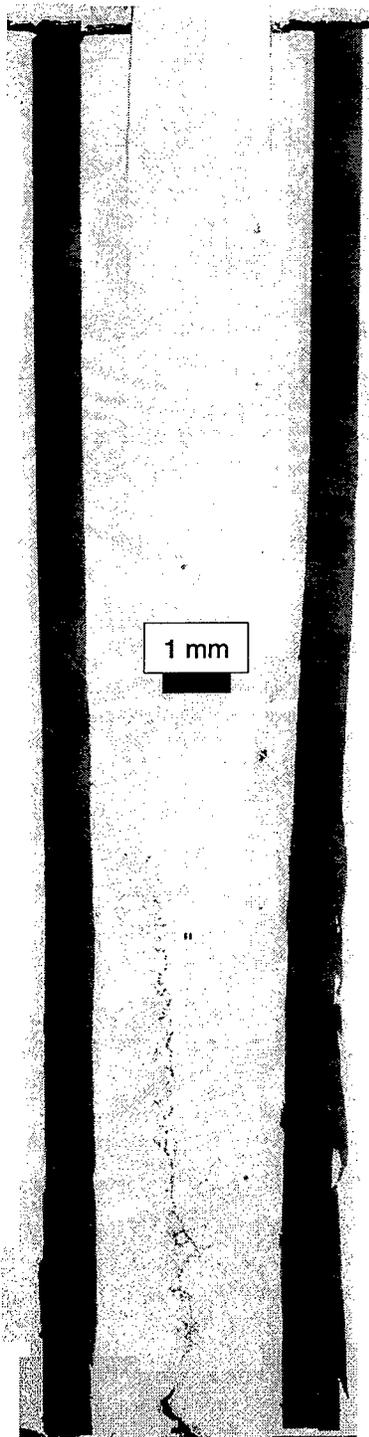
Figure 10. Longitudinal TWCM cross section.
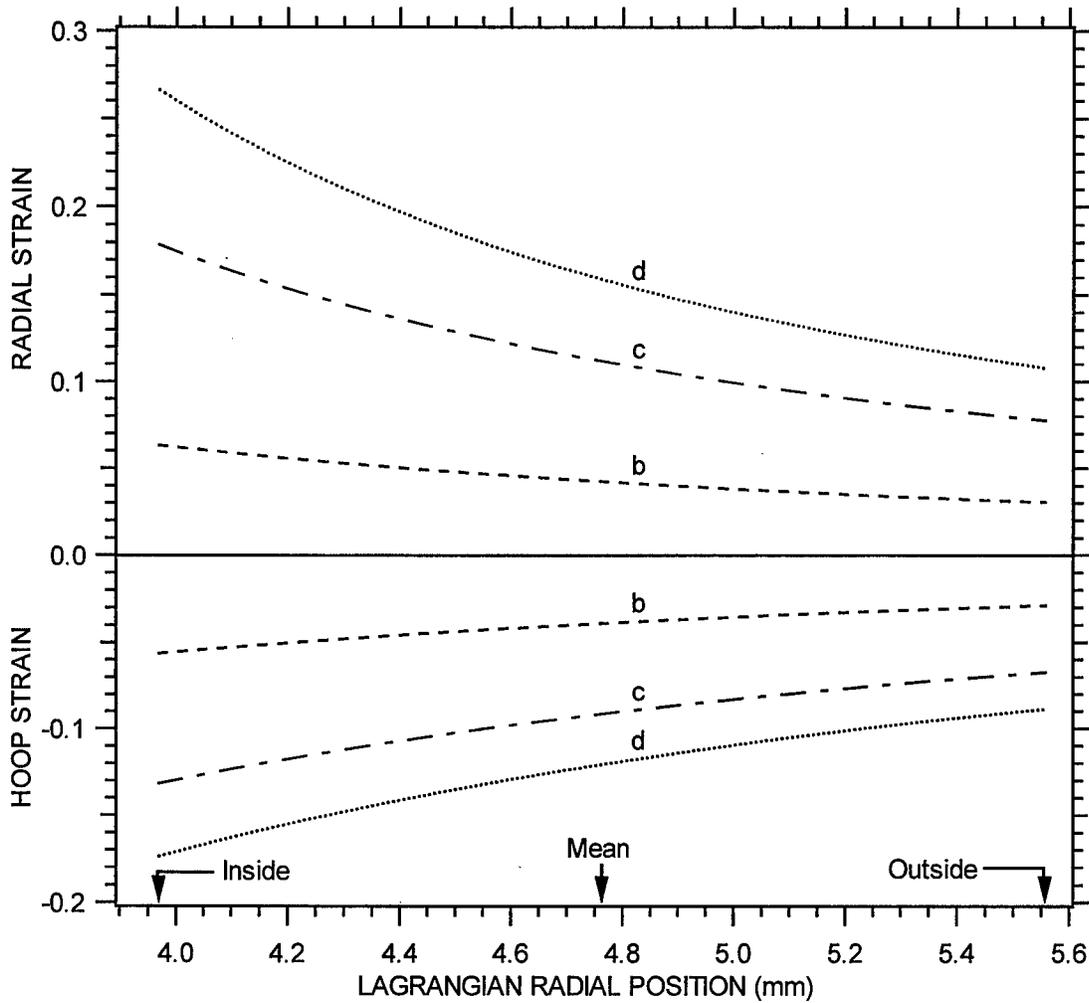
Figure 11. Finite Lagrangian strains in the ceramic for the cross sections shown in Figures 9b, c, and d, assuming incompressible, plane deformation. Inside, outside, and mean tube radii are indicated.

49
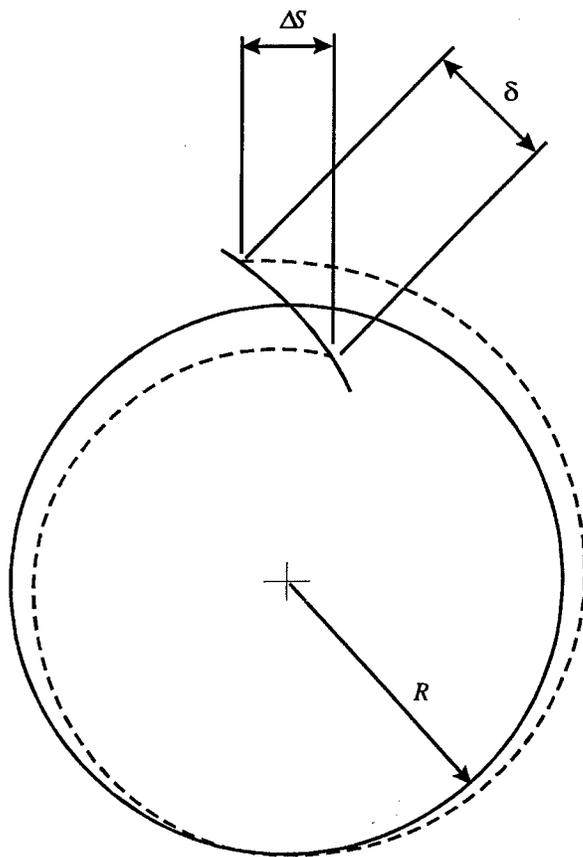
Figure 12. Graphical construction of the relationship between band slip and circumferential strain.

relationship between the circumferential strain and the displacement jump, δ, across the shear band is

$$\frac{\Delta S}{S} = \frac{\delta}{2\sqrt{2\pi}R} \approx \varepsilon_{\theta\theta} \approx \frac{u}{R} \tag{6-4}$$

where S is the circumference and u is the average radial displacement. Thus, when all of the deformation is accommodated by shear bands, the relationship between the average radial displacement and the displacement jump across each of N bands is

$$\delta = \frac{2\sqrt{2\pi}}{N}u \tag{6-5}$$

Figure 13 plots the displacement and displacement jump for the sections in Figure 9, assuming incompressible plane deformation and assuming that all of the deformation is accommodated in $N = 8$ identical bands. Displacement jumps at the section with the largest strain, Figure 9d, are computed to be around 700 μm.

SEM photographs of the same sections shown in Figure 9 were taken of individual shear bands, cracks, and relatively undeformed regions. From the SEM micrographs of the shear bands, shear band displacement jumps can be measured. In some cases, the size of the jump is different on the inside and the outside of the tube, implying that the material on one side of the band is stretched. This is particularly evident for the band on the left-hand side in Figure 14, in which there is virtually no step on the outside diameter and a large step on the inside diameter and many open cracks on the rhs of the band. Figure 15 is a magnified view of the cracked region.

The shear bands vary in character independently of where they are around its circumference or along the length of the tube, i.e., independently of the amount of strain. Some bands are very sharp and crack-like, e.g., Figure 16; some are more broad and diffuse, e.g., Figure 17; some are difficult to discern at higher magnification, e.g., Figure 18; some contain debris at their ends, e.g., Figure 19; and some do not, e.g., Figure 20.
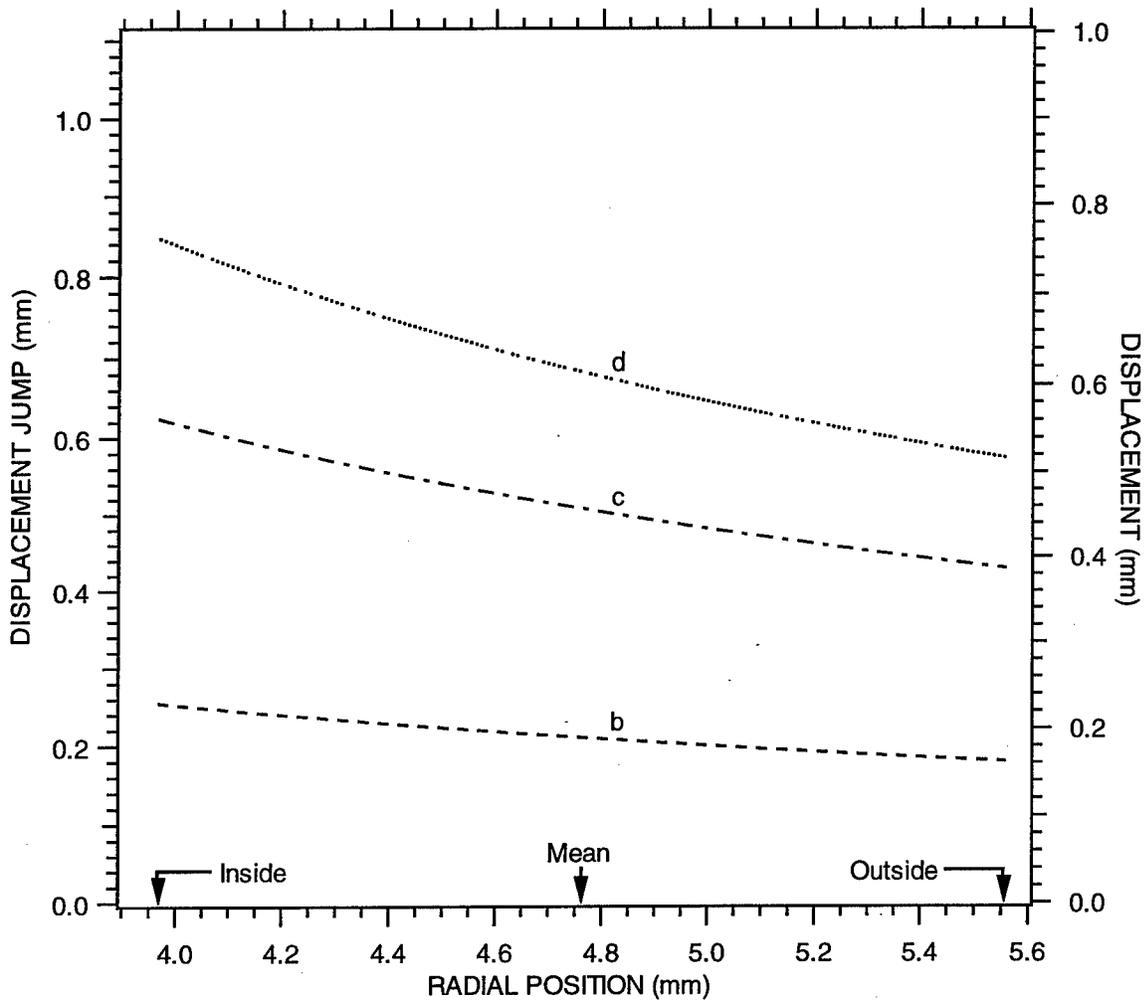
Figure 13. Shear band displacement jumps in the ceramic for the cross
sections shown in Figures 9b, c, and d, assuming 8 bands and
incompressible, plane, infinitesimal deformation. Inside, outside,
and mean tube radii are indicated.

300 μm ⊢─┤

Figure 14. Pair of shear bands with dilated region on the right-hand side of the left-hand band. $\varepsilon_{\theta\theta} \approx -0.12$.
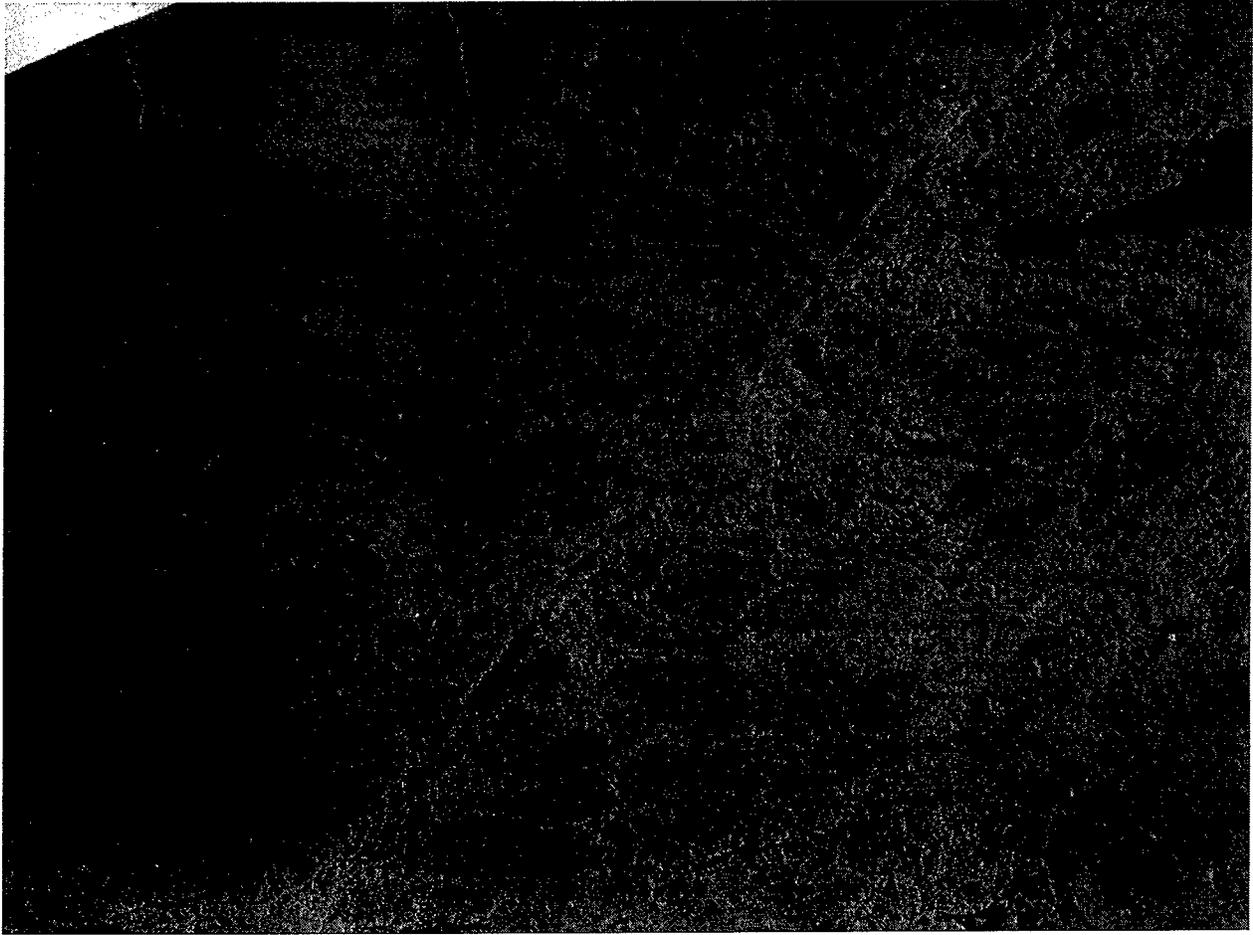
100 µm ⊢⊣

Figure 15. Magnified view of the dilated region in Figure 6.

$\varepsilon_{\theta\theta} \approx -0.04$

10 µm

$\varepsilon_{66} \approx -0.12$

10 µm
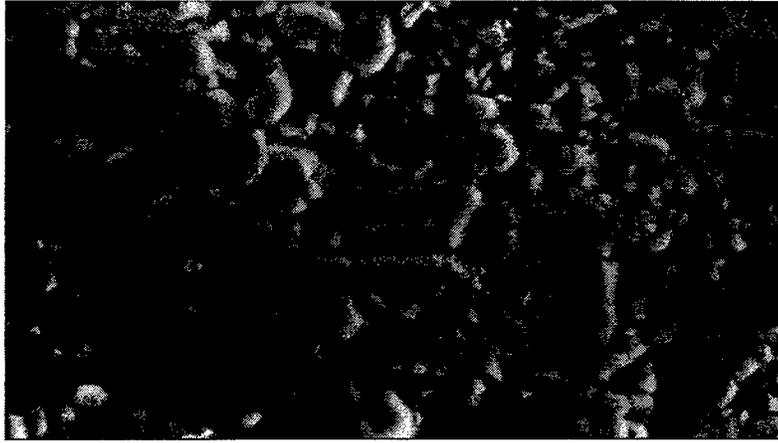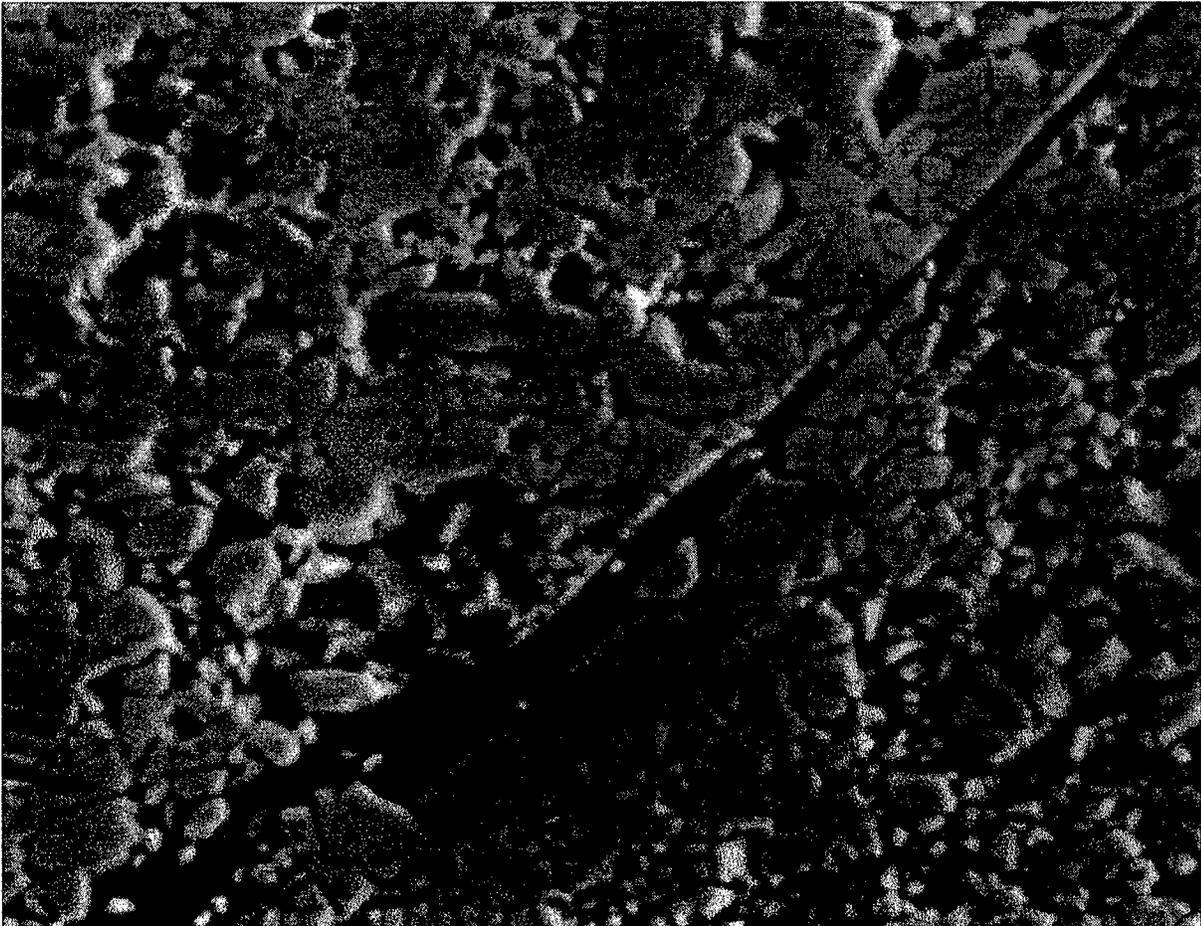
Figure 16. Sharp, highly localized shear bands.

55

100 μm ├─────┤

Figure 17. More diffuse shear band, $\varepsilon_{\theta\theta} \approx 0.12$.
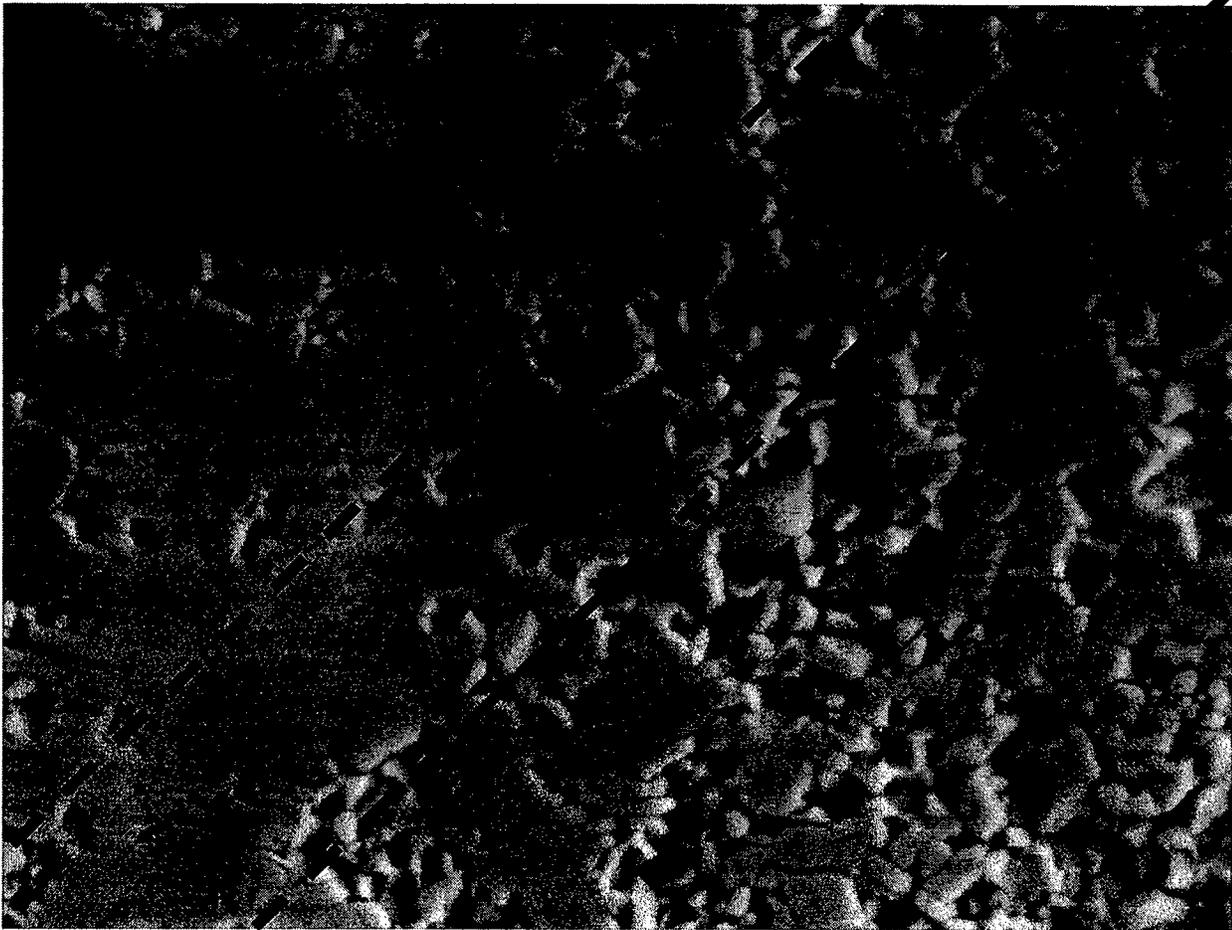
10 μm

Figure 18. High magnification view of shear band at $\varepsilon_{\theta\theta} \approx 0.04$. Band is located between the dashed lines.

10 µm |—|

Figure 19. Debris accumulated at OD end of the shear band at $\varepsilon_{\theta\theta} \approx 0.12$.
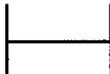
Figure 20. ID tip of shear band with minimal debris accumulation, $\varepsilon_{\theta\theta} \approx 0.12$.

Shear band quantity is relatively independent of the amount of deformation. Although the section taken where the core was solid (Figure 9a) has no bands, about 5 cracks are oriented roughly radially and spaced non-uniformly. About 10 bands are at the lowest level of compression (Figure 9b), with about 4 of those having significant shear steps on the ID or OD. About 8 bands are at the next level of compression (Figure 9c), all having significant shear. Finally, about 9 bands are at the highest level of compression (Figure 9d) with even more significant shear in each. Thus, the number of bands appears to be roughly constant at 8-10 spaced non-uniformly in the circumferential direction independently of the amount of inward compression.

Two-dimensional, free-Lagrange, hydrocode simulations of the experiment were performed using the FRAGBED2 implementation in the L2D hydrocode [13] to estimate the stress and strain rate conditions in the ceramic. The model included the explosive detonation. Two sets of simulations were performed. In one set, cylindrical axisymmetry was assumed, that is, the problem coordinates were the axial and radial directions. Figure 21 shows the mesh and Table 3 lists input parameters. The copper was modeled as Von Mises elastic-plastic. The axisymmetric model cannot capture the shear banding behavior and the simulation therefore provides only qualitative estimates of the average conditions in the ceramic.

Table 3

FRAGBED2 TWCM AND BALLISTIC SIMULATION PARAMETERS

Parameter	Symbol	Value	Units
Fracture Toughness	K_{IC}	4	$MPa\sqrt{m}$
Burgers Vector	b	0.01	
Initial Block Size*	B_0	3	μm
Initial Dislocation Density	N_{d0}	1.14×10^{10}	m^{-2}
Comminution Rate Saturation Width	m	1.5	
Relative Crack Size	η	0.01	
Max Crack Speed	C_R	496	m/s
Friction Coefficient	μ	0.3	

*±20% random variation introduced in plane strain simulation.
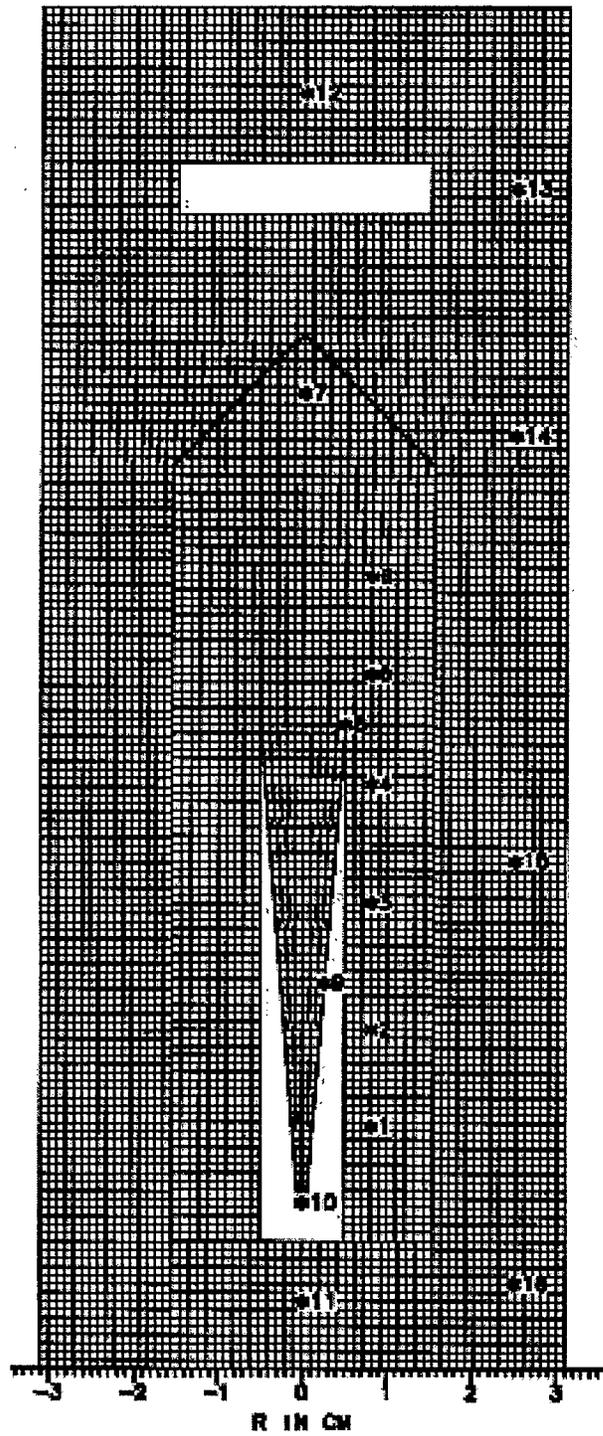
Figure 21. L2D mesh for axisymmetric FRAGBED2 simulations of the TWCM.
Numbers with asterisks indicate time history data plot points.

In the second set of simulations, plane strain deformation was assumed and the problem coordinates were the radial and circumferential directions (see Figure 22 and Table 3). The simulation corresponded to modeling the behavior of a single axial location, e.g., Figure 9d. As in the axisymmetric simulations, the copper was modeled as elastic-plastic, and the alumina was modeled using the FRAGBED2 model. The FRAGBED2 model uses an analogy to dislocation theory to describe the deformation of the ceramic. Fragments are imagined to slide on discrete planes at speeds controlled by the local stresses. Fragments can also reduce in size according to a comminution rate law. In an attempt to precipitate localization, a random ± 20% variation in initial fragment size and dislocation density was introduced in the axisymmetric simulations.

The results from the axisymmetric model show that the radial stress pulse is compressive and persists for about 10 μs and peaks around 4-8 Gpa; the circumferential stress pulse plateaus at about the input Hugoniot elastic limit for the ceramic, 6 Gpa, and has a duration of up to 15 μs; and the axial stress is compressive, about 2 Gpa in magnitude, and persists for about 25 μs. The radial velocity is around 1.5 m/s inward. Radial strains are overall positive and vary from 0% to 20% along the taper section, and the radial strain rate is about 2×10^4 s^{-1}. Hoop strains are compressive and vary up to -15% at similar rates. Axial strains are at most 5%. Figure 23 shows strain paths in the r-θ plane.

The fact that the radial stress pulse is 5 μs shorter than the circumferential stress pulse and 10 μs shorter than the axial stress pulse may explain some of the propensity for shear banding and the radially stretched region on the right side of the band in Figures 14 and 15. The circumferential and axial stresses remain high after the radial stress falls off, which places the ceramic in a state of biaxial compression. The reduced stress in the radial direction implies that the ceramic might be able to expand in the radial direction and that faulted blocks might be able to slide off each other in the radial direction.

The deformation computed in the plane strain, FRAGBED2 model shows only slight tendency to localize into logarithmic spiral shear bands. As shown in Figures 24 and 25, there are indications of localized comminution and localized deformation, but the localization is of a different form and more diffuse than observed in the experiments, and might be related to the fact that fragment dislocations are restricted to move on a set of discrete planes, rather than the emergence of a true softening instability. It might also be related to the fact that in the plane strain simulation there is a strong radial shock, whereas in the TWCM test the wave sweeps down the length of the ceramic tube. In the simulation, the radial motion rebounds strongly after
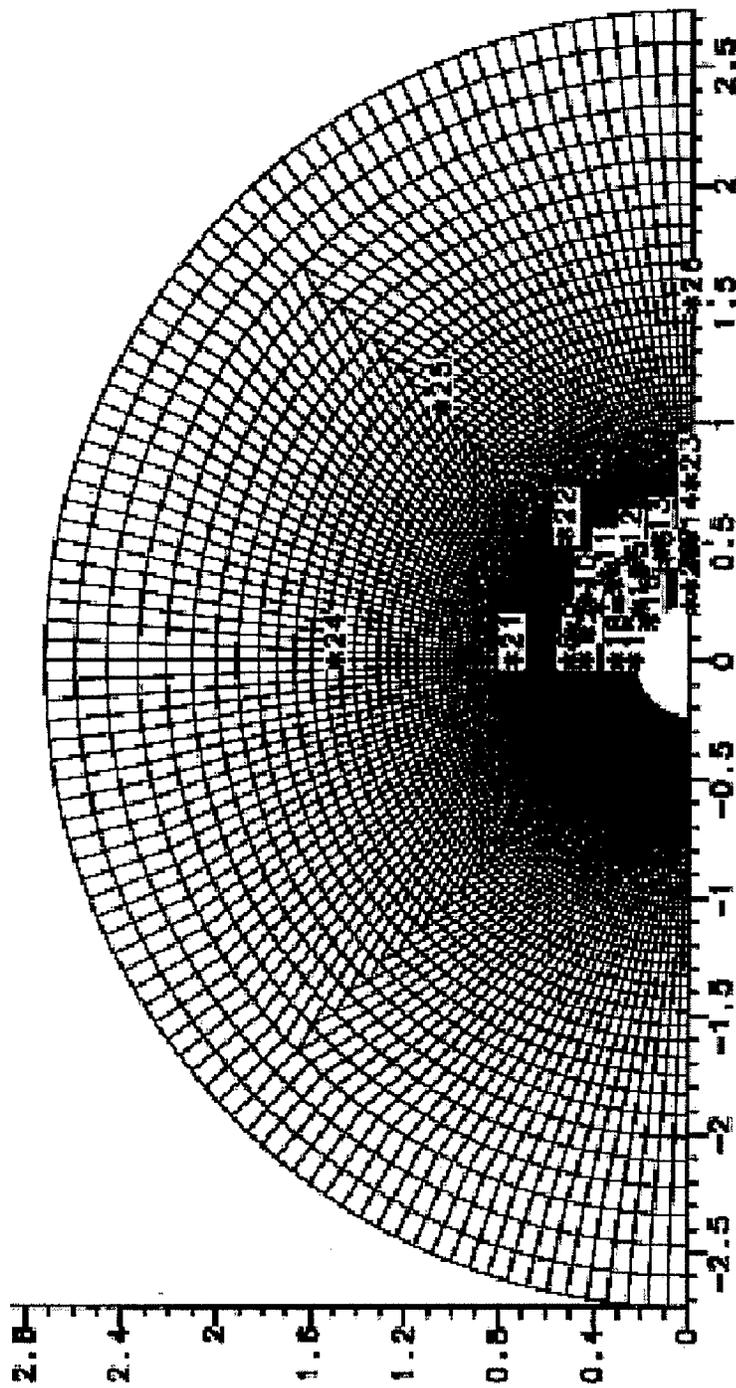
Figure 22. L2D mesh for plane strain FRAGBED2 simulations of the TWCM.
Scale in centimeters. Numbers with asterisks indicate time history data plot points.
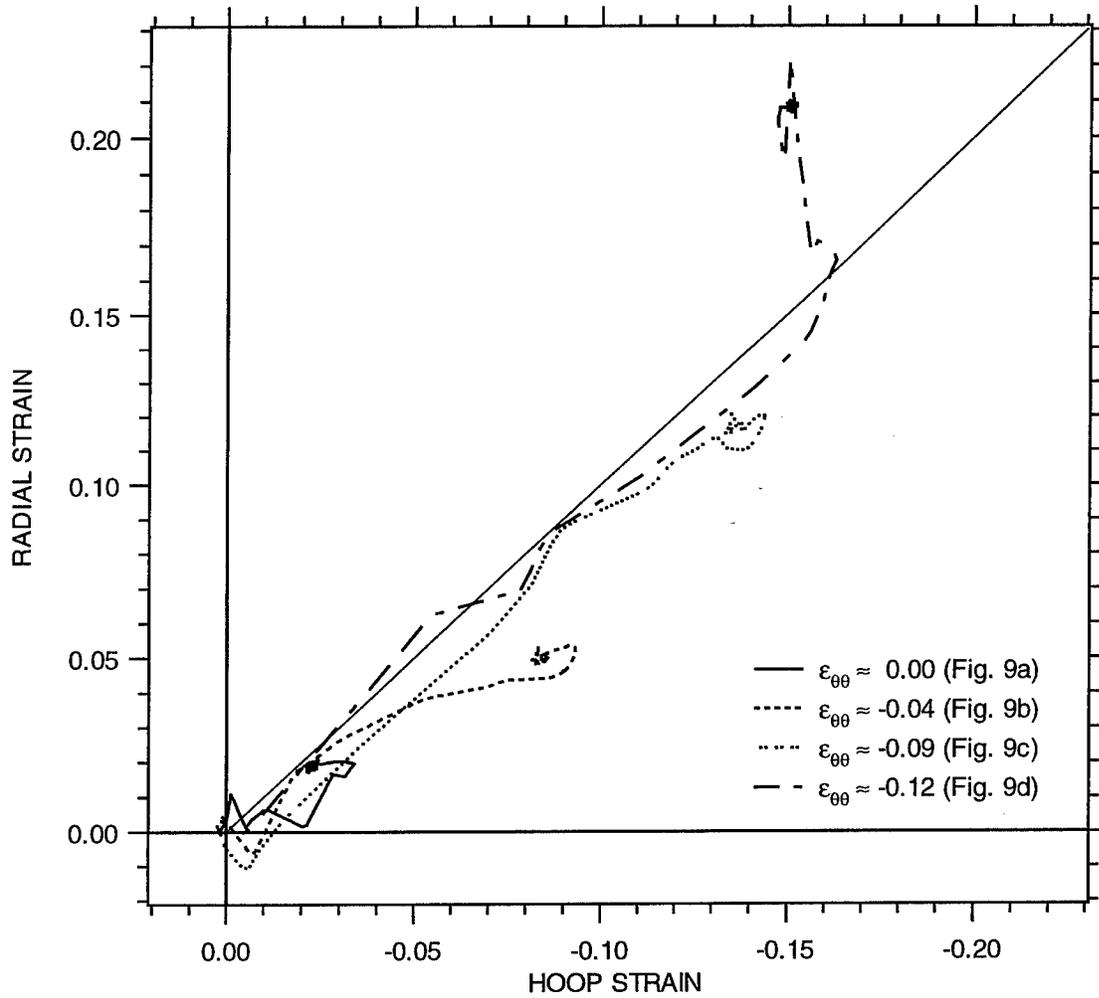
Figure 23. Strain paths corresponding to Figure 9 cross sections obtained from L2D axisymmetric simulations.
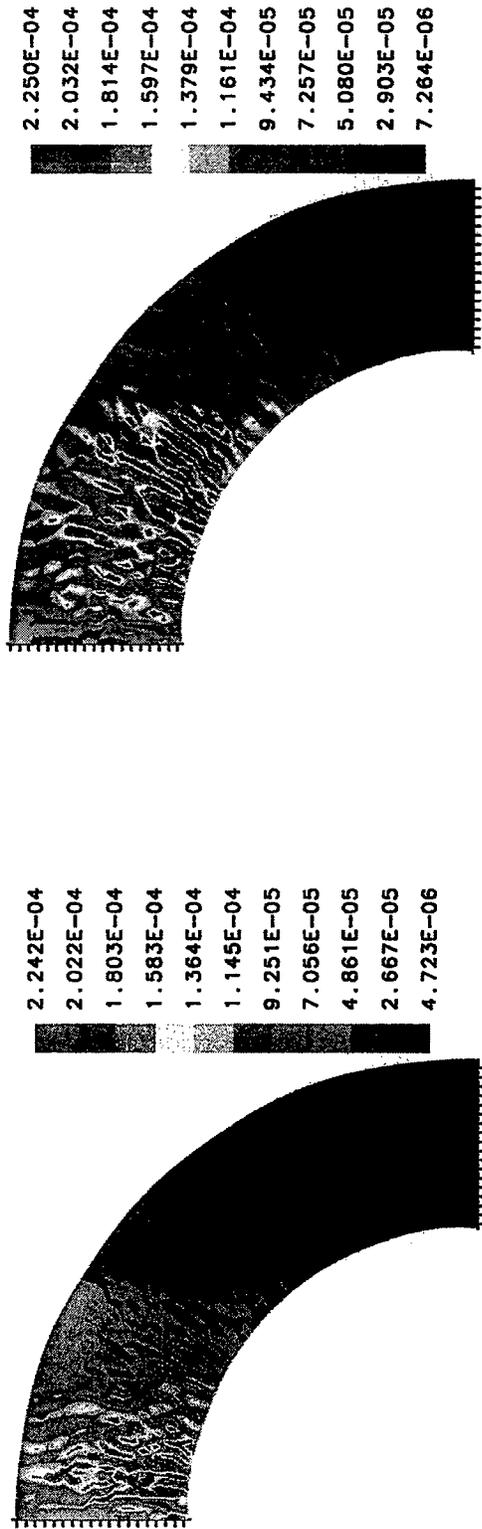
2.250E-04	
2.032E-04	
1.814E-04	
1.597E-04	
1.379E-04	
1.161E-04	
9.434E-05	
7.257E-05	
5.080E-05	
2.903E-05	
7.264E-06	

67.5°

2.242E-04	
2.022E-04	
1.803E-04	
1.583E-04	
1.364E-04	
1.145E-04	
9.251E-05	
7.056E-05	
4.861E-05	
2.667E-05	
4.723E-06	

90°

Figure 24.   Contour plots of FRAGBED2 blocksize, B, at $t = 8$ μs for slip planes with normals at 90° (vertical), 67.5°, 45°, and 22.5°. (continued)
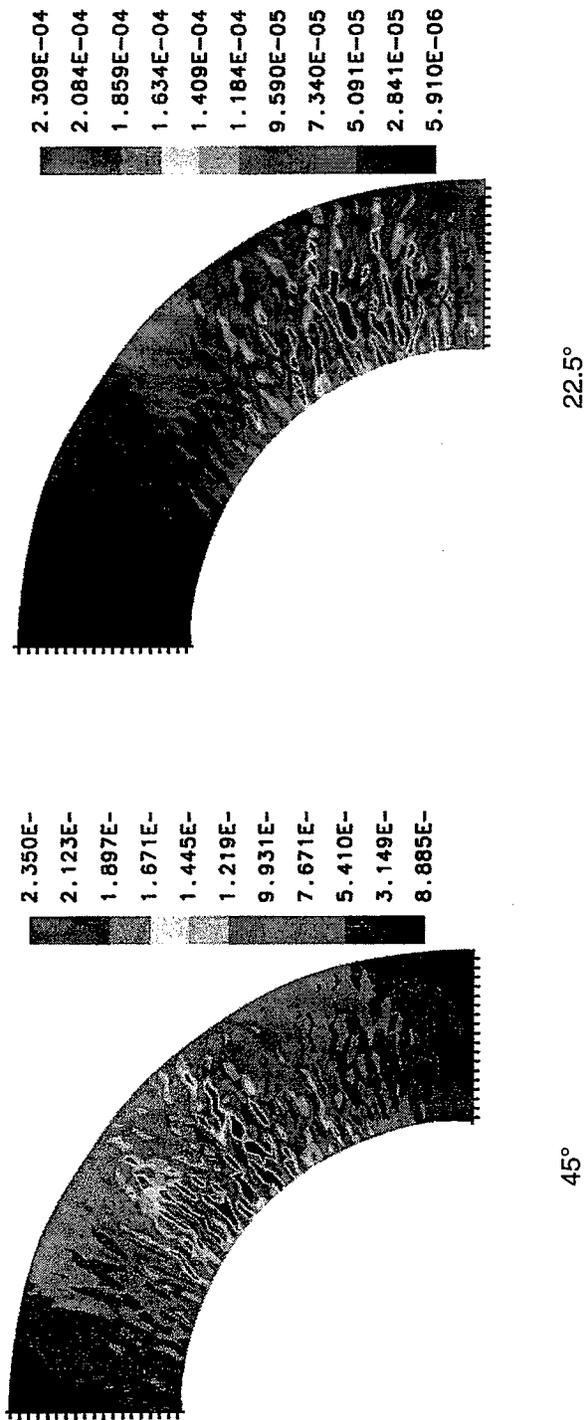
65

Figure 24. Contour plots of FRAGBED2 blocksize, B, at $t = 8$ µs for slip planes with normals at 90° (vertical), 67.5°, 45°, and 22.5°. (concluded)
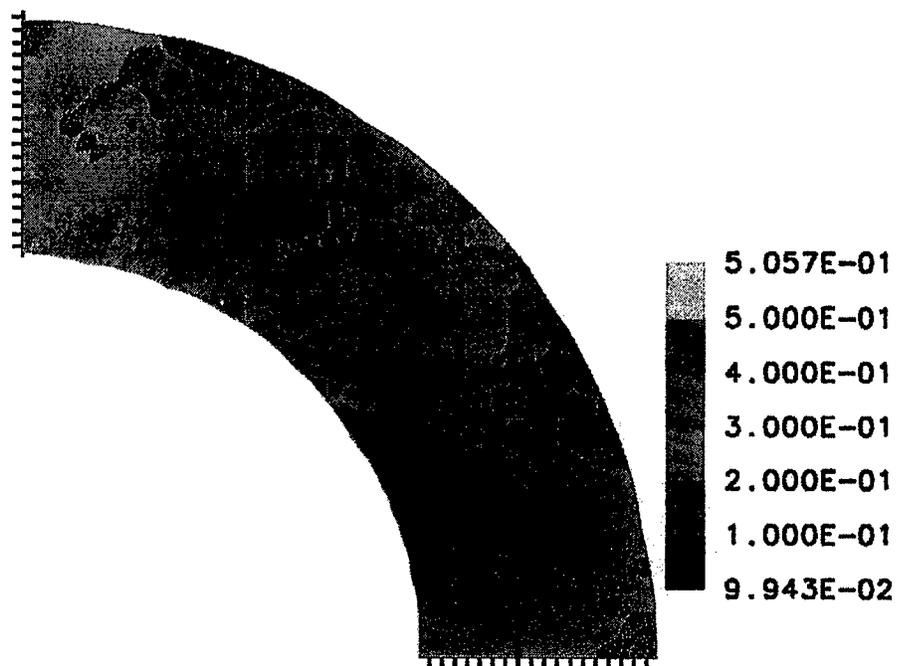
Figure 25. Contour plot of FRAGBED2 equivalent plastic strain at $t = 8$ μs.

the inner copper tube contacts the central pin, but there is no evidence of rebound in the TWCM assemblies sectioned posttest (see Figures 9 and 10). The sweeping motion combined with the shear localization makes the TWCM fully three-dimensional. Thus, plane strain simulations are not completely faithful representations of the true deformation. Perhaps the sweeping motion helps trigger localization. On the other hand, the experimental rock mechanics literature contains instances of quasistatic and dynamic plane strain radial compression of holes leading to spiral shear bands.

The transverse sections show clearly that shear localization or faulting is a significant mechanism by which the hoop compression is accommodated, even at the smallest levels of hoop compression (Fig. 9b). However, the displacement jumps in Figure 9 are significantly smaller than those estimated as if all the deformation were by shear banding (Figure 13), which implies that, indeed, not all of the deformation is accommodated by the bands. Another significant mechanism must be present for accommodating hoop compression. Given the fragmentation visible in Figure 9 and 10, and given the low amount of atomic dislocation plasticity observed in other explosively loaded alumina samples [32], shifting, rearrangement, and breaking of fragments appears to be a likely mechanism.

The transverse section taken where the core was solid and where there was therefore only minimal straining shows radial cracks (Figure 9a) that could immediately lead to the shear banding mechanism with further compression. For instance, a detail of one of these cracks, Figure 26, shows that it is curved and that further compression could be accommodated by sliding along the crack faces.

Chen and Ravichandran [33] performed split-Hopkinson bar compression tests on glass-ceramic cylinders surrounded by thick metal jackets intended to provide radial confining stress. All of their confined cylinders failed by faulting, and the faulting appeared to begin at the earliest stages of the deformation. As was the case for TWCM, there seemed to be little or no homogeneous inelastic deformation prior to the onset of faulting. In contrast with TWCM, however, the amount of debris in the fault slip region seemed to correlate with the amount of slip.

Nesterenko et al. applied the untapered TWCM to compacted ceramic powders [30]. Compared with the results obtained here, the powder tests produce many more bands and the bands are more uniform in displacement jump and spacing. The same is true for Nesterenko's test on ceramic subjected to two explosions. In either case, more than 50 bands were produced at an average circumferential strain around -0.2. As in the work reported here, Nesterenko et al. [30]

100 µm ⊢

Figure 26.   Curved crack in section with solid core, $\varepsilon_{\theta\theta} \approx 0$.

found that significant portions of the total deformation were accommodated by mechanisms other than shear banding.

The flowing fragment bed picture of ceramic deformation differs from the shear localization picture observed in the TWCM tests. Which picture applies to ceramic armor penetration is an important issue. Apparently, both pictures apply, perhaps at different stages in the penetration process. This issue has strong implications for armor design, modeling, and choice of experiments for characterizing penetration resistance.

The preponderance of shear bands and the fact that even the smallest levels of radial compression result in cracks that could become bands suggest that, under the geometry, stresses, strain, and loading rate conditions under consideration, shear banding is a significant mechanism by which the ceramic deforms. However, fragment flow also appears to be a significant mechanism.

BALLISTIC TESTS

Subramanian and Bless [34] have performed a series of ballistic experiments in which they shot confined AD-995 alumina cylinders against stationary L/D=20 tungsten rod penetrators in the reverse ballistics mode. Penetration and rod erosion histories were recorded using flash x-rays. We simulated their tests at 1.5 and 3.5 km/s using FRAGBED2 in L2D, with the same set of parameters for both simulations. Parameter values are shown in Table 3. Figure 27 shows the computational mesh at a stage part way through a penetration. Figure 28 shows the computed penetrator tip and tail trajectories for the two simulations, along with average steady-state velocities reported by Subramanian and Bless [34]. At 1.5 km/s, the computed penetration rate is well within the scatter band of the measured rates. At 3.5 km/s, computed rates are barely within the low side of the scatter band, about 15% below the mean of the measured rates.

The computed results are sensitive to initial fragment size and to the initial porosity. Subramanian and Bless claim an initial porosity for their AD-995 of around 2%. Our microscopic observations of AD-995 indicate a porosity well below 5%. Based on the ratio of the manufacturer's reported density for AD-995, 3.89 g/cm^3, to that of α-alumina, 3.97 g/cm^3, we also estimate the porosity to be around 2%. In any case, we found that FRAGBED2, with an initial porosity around 2%, gave the best match to the ballistic experiments of Subramanian and Bless.
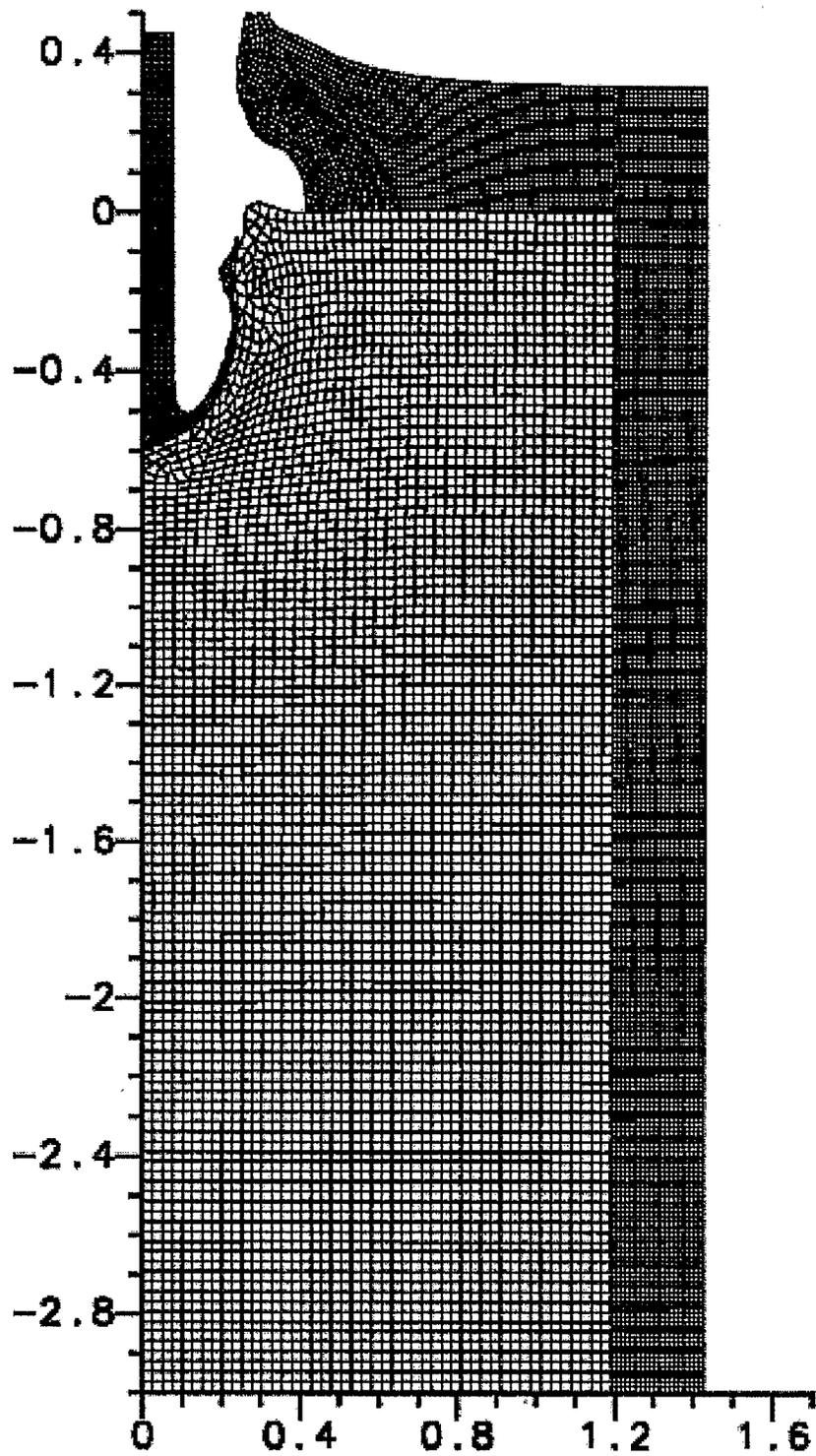
Figure 27. FRAGBED2/L2D simulation of tungsten long rod penetration in AD-995 alumina. Scale is in centimeters.

71
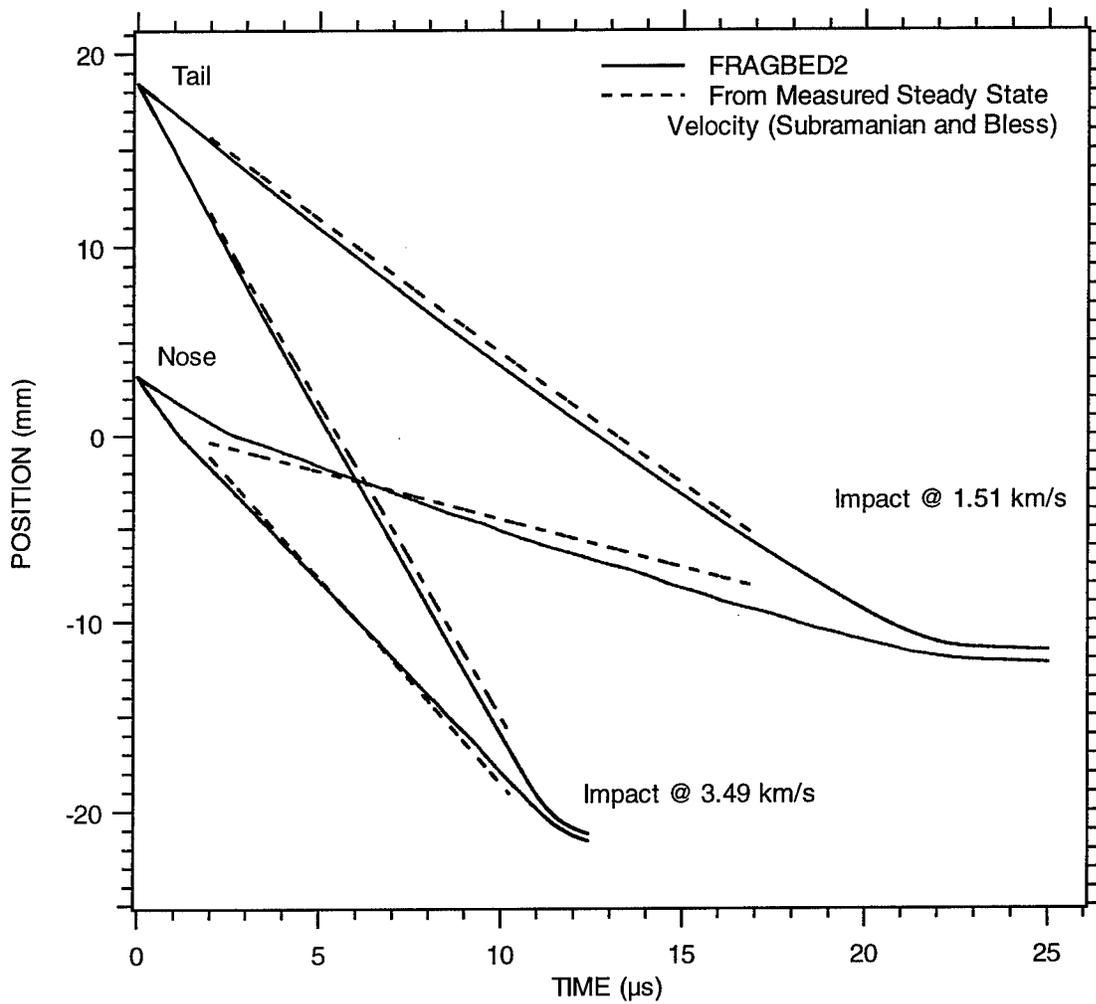
Figure 28   Comparison of FRAGBED2 and measured [34] steady-state
penetration velocities. The cover plate occupies from 3 to 0 mm along the
position axis and the ceramic extends from 0 to -51 mm.

72

SECTION 7

DISCUSSION AND CONCLUSIONS

In this section, we list the FRAGBED2-specific input parameters and discuss the importance of each in determining key aspects of penetration or cratering behavior. FRAGBED2 requires the following FRAGBED2-specific input parameters. (Non-FRAGBED2-specific parameters include the solid density and the solid moduli.)

Table 4

FRAGBED2 PARAMETERS

Parameter	Description	Comments
No. and orientation of planes	Arbitrary; can be tailored to each problem	All non-elastic slip occurs on these planes.
B_0(cm)	Characteristic fragment granule size at onset of granular flow and comminution	This parameter is determined from fracture calculations or algorithms.
N_{∞} (no./cm^2)	Initial dislocation density (number/unit area)	Depends on boundary and initial conditions
b	Dislocation jog coefficient	Related to granule morphology
μ	Coefficient of friction between granules	Normally based on handbook values
h, m	Comminution parameters	Chosen by correlation with cavity expansion experiments
g	Granule geometry factor	Normally set to unity
K_{1D}(dyne cm$^{-3/2}$)	Solid dynamic fracture initiation toughness	Normally based on handbook value
m_1, m_2	Local stress factor coefficients	Related to granule morphology

All ten parameters in the above table can be in principle assigned different values on each plane of this multiplane model. (This is in fact an important capability for cases in which pre-

73

existing interfaces or planes of weakness exist in the material.) The total number of potential input parameters is thus equal to 10 times the number of planes used in the model. For example, in the L2D applications discussed above we used 13 planes, so the number of potential parameters in that case is 130.

However, in initially isotropic cases, we use the same parameters on all planes. Thus, in many if not most armor ceramic applications (such as the examples shown in this report), the number of FRAGBED-specific, input material, property parameters is 10.

The effects of varying input parameters in FRAGBED2 are difficult to predict *a priori* because of the many interactions between different parts of the model. In a parametric study leading to the correlation between computations and experimental data discussed above, we varied all the above input parameters except g (assumed to be unity) and K_{ID} (set to $4 \text{ MPa} \sqrt{m}$). The results showed that, as hoped, they depended on the input parameters in a stable way, i.e., modest changes in the input cause only modest changes in the output.

In conclusion,

- The FRAGBED2 model treats the physics relevant to ceramic armor penetration: fracture, comminution, and flow of the fragmented bed.

- FRAGBED2 models reasonably well laboratory experiments in which alumina armor was impacted by tungsten long rods.

- FRAGBED2 correctly models particle velocity histories obtained in spherical cavity expansion experiments.

- FRAGBED2 predictions are sensitive to readily identifiable and measurable material parameters, such as initial fragment size, fracture toughness, and friction coefficient.

- We have not found a set of FRAGBED2 parameters that would allow it to predict the shear bands observed in TWCM tests performed on alumina.

- The deformation in TWCM tests on alumina is accompanied by both shear bands and by fragment flow.

ACKNOWLEDGMENTS

PUBLICATIONS AND PRESENTATIONS

1. J. T. McGinn, R. W. Klopp, and D. A. Shockey, "Deformation and Comminution of Shock Loaded α-Al_2O_3 in the Mescall Zone of Ceramic Armor," *Mat. Res. Soc. Proc.* 362 61-66 (1995).

2. D. R. Curran, L. Seaman, J. W. Simons, and T. Cooper, "Modeling the Flow of Fragmented Brittle Material," Proceedings of the International Conference on Computational Engineering Science, July 30- August 5, 1995, Hawaii.

3. R. W. Klopp, D. R. Curran, D. A. Shockey, and T. Cooper, "A Comminution Model for Penetration in Ceramics," Presented at the 14th Army Symposium on Solid Mechanics, Myrtle Beach, South Carolina, October 16-18, 1996.

INVENTIONS

There were no inventions conceived under the auspices of this project.

PARTICIPATING SCIENTIFIC PERSONNEL

Donald A. Shockey, Associate Director and Principal Investigator

Richard W. Klopp, Research Engineer III

Donald A. Curran, Senior Staff Scientist

Thomas Cooper, Principal Applications Programmer

Christine Kanazawa, Materials Scientist II

Anastasia Canazales, Materials Chemist II

Vitali F. Nesterenko, Professor, University of California, San Diego (assisted with Thick-Walled Cylinder method)

REFERENCES

1. D. A. Shockey, A. H. Marchand, S. R. Skaggs, G. E. Cort, M. W. Burkett, and R. Parker, "Failure Phenomenology of Confined Ceramic Targets and Impacting Rods," *Int. J. Impact Engng.* 9, 263-275 (1990).

2. D. R. Curran, L. Seaman, T. Cooper, and D. A. Shockey, "Micromechanical Model for Comminution and Granular Flow of Brittle Material Under High Strain Rate Applicatoin to Penetration of Ceramic Targets," *Int. J. Impact Engng.* 13(1), 53-83 (1993) .

3. S. B. Batdorf and B. Budianski, "A Mathematical Theory of Plasticity Based on the Concept of Slip," *Tech. Note No. 1871 of the National Advisory Committee for Aeronautics*, Washington, DC (April 1949).

4. D. R. Curran, L. Seaman, and D. A. Shockey, "Dynamic Failure of Solids," *Physic Reports,* 147, Nos. 5 and 6 (1987).

5. Z. Bazant and W. P. Murphy, in *Constitutive Laws for Engineering Materials*, C. S. Desai, E. Krempl, G. Frantziskonis, and H. Saadatmanesh, Eds., pp. 377-384, ASME Press, New York (1991).

6. S. Nemat-Nasser and M. Hori, *Micromechanics: Overall Properties of Heterogeneous Materials*, North-Holland, Amsterdam (1993).

7. J. W. Simons, T. H. Antoun, and D. R. Curran, "A Finite Element Model for Analyzing the Dynamic Cracking Response of Concrete," in *Proceedings of the 8th International Symposium on the Effects of Munitions with Structures,* McLean, Virginia (April 22-25, 1997).

8. A. M. Rajendran, "A Review of Constitutive/Damage Models for Ceramic Materials in Hydrocodes," in *Proceedings of the International Workshop on New Models and Numerical Codes for Shock Wave Processes in Condensed Media*, St. Catherine's College, Oxford (15-19 September 1997).

9. M. E. Kipp and D. E. Grady, "Experimental and Numerical Studies of High-Velocity Impact Fragmentation," in *High Pressure Shock Compression of Solids II*, Dynamic Fracture and Fragmentation, Lee Davison, D. E. Grady, and M. Shahinpoor, Eds., pp. 283-339, Springer, Heidelberg (1995).

10. E. Orowan, "Zur Kristallplastizitat III. Über den Mechanismus des Gleitvorganges," *Z. Phys.* 89, 634-659 (1934).

11. W. Weibull, "A Statistical Theory of the Strength of Materials," *Ing. Vetensk. Akad. Handl.*, 151, 5-45 (1939).

12. S. Wolfram, *Mathematica: A System for Doing Mathematics by Computer* Addison-Wesley, Reading, Mass. (1991).

13. T. Cooper, "Manual for the TDL Wave Propagation Code for Large Deformation Problems," Technical Report, SRI International (1990).

14. L. S. Costin, "Damage Mechanics in the Post-Failure Regime," *Mechanics of Materials*, 4, 149-160 (1985).

15. D. Peirce, R. J. Asaro, and A. Needleman, "Material Rate Dependence and Localized Deformation in Crystalline Solids," *Acta Metall.* 31(12), 1951-1976 (1983).

16. L. E. Malvern, *Introduction to the Mechanics of a Continuous Medium*, Prentice-Hall Inc., Englewood Cliffs, New Jersey (1969).

17. B. D. Coleman and M. E. Gurtin, "Thermodynamics with Internal State Variables," *J. Chem. Phys.* 47(2), 597-613 (15 July 1967).

18. G. B. Whitham, "Some Comments on Wave Propagation and Shock Wave Structure with Application to Magnetohydrodynamics," *Communications on Pure and Applied Math*, XII, 113-158 (1959).

19. G. B. Whitham, *Linear and Nonlinear Waves*, John Wiley and Sons, New York (1974).

20. R. W. Klopp, D. A. Shockey, L. Seaman, D. R. Curran, J. T. McGinn, and T. de Resseguier, "A Spherical Cavity Expansion Experiment for Characterizing Penetration Resistance of Armor Ceramics," *Mechanical Testing of Ceramics and Ceramic Composites*, AMD-Vol 197, ASME, New York (1994).

21. D. R. Curran, L. Seaman, R. W. Klopp, T. de Resseguier, and C. Kanazawa, "A Granulated Material Model for Quasibrittle Solids," in *Fracture and Damage in Quasibrittle Structures*, Z. P. Bazant , Z. Bittnar, M. Jirasek, and J. Mazars, Eds., E & FN SPON, London (1994).

22. G. Raiser, "High Strain rate Deformation and Damage in Ceramic Materials," *J. Engrng Materials Technology* 115(3), 292-299 (1993).

23. G. Johnson and T. Holmquist, "An Improved Computational Constitutive Model for Brittle Materials," in *High-Pressure Science and Technology - 1993, Part 2*, AIP Press, 981-984 (1994).

24. A. M. Rajendran and D. J. Grove, "Modeling the Shock Response of Silicon Carbide, Boron Carbide, and Titanium Diboride," *Int. J. Impact Engng.* 18(6), 611-631 (1996).

25. H. D. Espinosa, "On the Dynamic Shear Resistance of Ceramic Composites and its Dependence on Applied Multiaxial Deformation," *Int. J. Solids Structures* 32(231), 3105-3128 (1995).

26. V. F. Nesterenko, A. N. Lazaridi, and S. A. Pershin, *Fiz. Goreniya Vzryva* 25, 154-155 (1989).

27. V. F. Nesterenko and M. P. Bondar, "Investigation of Deformation Localization by the 'Thick-Walled Cylinder' Method," *DYMAT Journal* 1(3), 245-251 (1994).

28. V. F. Nesterenko, M. A. Meyers, and T. W. Wright, "Collective Behavior of Shear Bands," *Metallurgical and Materials Applications of Shock-Wave and High-Strain-Rate Phenomena*, L. E. Murr, K. P. Staudhammer, and M. A. Meyers, eds. (Elsevier Science B. V., Holland) 397-404 (1995).

29. V. F. Nesterenko, M. A. Meyers, H. C. Chen, and J. C. LaSalvia, "Controlled High-Rate Localized Shear in Porous Reactive Media," *Appl. Phys. Lett.* 65(24), 3069-3071 (1994).

30. V. F. Nesterenko, M. A. Meyers, and H. C. Chen, "Shear Localization in High-Strain-Rate Deformation of Granular Alumina," *Acta Mater.* 44(5), 2017-2026 (1996).

31. V. F. Nesterenko, "Controlled High-Rate-Strain Shear Bands in Inert and Reactant Porous Materials," *Proc. 1997 Topical Conference on Shock Compression of Condensed Matter*, Amherst, Mass. (27 July - 1 August 1997),

32. J. T. McGinn, R. W. Klopp, and D. A. Shockey, "Deformation and Comminution of Shock Loaded α-Al_2O_3 in the Mescall Zone of Ceramic Armor," *Mat. Res. Soc. Proc.* 362 61-66 (1995).

33. W. Chen and G. Ravichandran, *J. Mech. Phys. Solids* 45(8), 1303-1328 (1997).

34. R. Subramanian and S. J. Bless, "Penetration of Semi-Infinite AD995 Alumina Targets by Tungsten Long Rod Penetrators from 1.5 to 3.5 km/s," *Int. J. Impact Engng.* 17, 807-816 (1995).

APPENDIX: NUMERICAL DEFINITIONS AND ROUTINES

DEFINITIONS

Block size = initial block size in centimeters. There is only one initial block size, common for all planes. No default.

Burger = burgerís vector, non-dimensional. No default.

Coheslip = initial cohesion on all slip planes in MBar. Default zero.

Crayleig = Rayleigh wave velocity in cm/μs. No default.

Dislocde = initial dislocation density on all planes in cm^{-2}. No default.

Elastic: elastic only calculation. No slip on planes. For testing purposes.

Endsub: end of FRAGBED input.

Eta = η in the comminution model, dimensionless. No default.

Ftoughne = fracture toughness in MBar│cm. No default.

Gsmall = g in the formula for the plastic strain rate on a slip plane, dimensionless. No default.

Initfp: non-trivial initialization of the plastic deformation tensor Fp. Ordinarily Fp is initialized to unity. This flag will make the code initialize Fp to a non-trivial value that is hard-wired in the code (look for the string NON-TRIVIAL FP). For testing purposes.

M1 = the shear stress factor in the driving stress formula, dimensionless. No default.

M2 = the normal stress factor in the driving stress formula, dimensionless. No default.

Mufricti = the coefficient of friction on all planes, dimensionless. No default.

Notslip: ordinarily two pairs of out-of-plane planes allow slip that limits the out-of-plane shear stresses. This flag will limit the planes to the ones that the user specifies in the x-y plane. Setting NOTSLIP in a 2D problem would cause all slip to occur on planes with normals in the x-y planes. This would result in unlimited shear strength in the two tangential directions. For testing purposes and true 3D problems. For 3D simulations, the user should always set the planes manually.

Notransp: turns off the dislocation transport on all planes. For testing purposes.

Nslip = number of slip planes. In 2D, these are the planes that the user specifies. Do not include the default out-of-plane planes. In 3D, remember to set the notslip flag above. No default.

Satwidth = the m parameter in the saturation and threshold stress formulas in the comminution model, dimensionless. No default.

Snormal(I) = Nx Ny Nz
   I = plane number (1 through nslip). No default.
   (Nx,Ny,Nz) is the slip plane normal. The code will normalize the vector. No default. Always three values. In 2D, Nz should be zero.

ROUTINES

SUBROUTINE FRAGB(IERR,LUUT,NCALL,DELTC,EQ,SDEV,FD,FPI,EXC,HEPS,
PCUT,S,EXM,LABEL,RLABEL,JPOSN,LM3,NUM)

This is the main subroutine for the FRAGBED model. This is the only routine that the simulation code needs to interface. There are essentially three times when the simulation code needs to call FRAGB: at material model parameter setup, at internal state variable setup, and at calculation of the stress from the deformation. See NCALL below.

FRAGB Arguments

In the following INTEGER and REAL*8, refer to FORTRAN programming syntax. REAL*8 is called double precision on most computers.

INTEGER IERR: negative for error. Initially set to 0 by FRAGB. Returns storage used by the EXM and EXC arrays.

INTEGER LUUT: FORTRAN logical unit number for the general output file. Should be set at any call.

INTEGER NCALL:
  0 for material model setup. The material model parameters must be supplied via LABEL, RLABEL, etc. for this call. The number of REAL*8 words needed for the material model parameters in the array EXM is returned in IERR.
  1 for initialize internal state variables. The number of REAL*8 words needed for the material model parameters in the array EXC is returned in IERR.
  2 for compute new stress tensor given new deformation tensor FD. This is the critical point for this model. Everything in the finite difference update scheme is updated in this call.

However, the dislocation transport requires one immediately preceding call to load transport variables and one immediately succeeding call to unload the updated transport variables.

3 for return slip plane variables in the array EQ. For this call, EQ must be an array of at least dimension NSLIP*7+2. Where NSLIP is the maximum number of slip planes possible in the model (not the particular number of slip planes for this case). This call can be used to extract information for contour plots, time histories, etc.

4 for load transport variables. When updating the dislocation transport, the scheme must have information about the internal state variables for the cell neighbors to the cell that we are currently processing. Also needed are the normal vector and surface area of the interface between the current cell and the respective neighbor. This information about the neighbors is transferred via the RLABEL and LM3 variables borrowed for this purpose. The information is stored internally in the subroutine in static variables. This call must be immediately preceding the compute call above (NCALL=2).

5 for unload transport variables. The dislocation density is returned for all the neighbor cells that have been updated. The dislocation density for the current cell itself is returned as part of the compute call above (NCALL=2). This call must immediately succeed the compute call above (NCALL=2).

6 for return plastic deformation tensor rigid body angle. This is part of the rezoning calls described below. The rezoning is by necessity very code dependent. Also, the call only applies to 2D, because in 3D there are three angles.

7 for backcalculate Fe from F and Fp for rezoning purposes.

8 for do the rezoning.

9 for after rezone clean up.

10 for printing a summary of the internal state variables on the file connected to logical unit LUUT. The printout is 80 column wide. There is one printout for every call to FRAGB, i.e., the caller must loop over all the cells for which a printout is desired.

REAL*8 DELTC: the current timestep of the finite difference scheme.

REAL*8 EQ: array whose dimension varies with the call. The general use is to provide information for the pressure equation of state. The details depend on the model. In the L2D code, EQ provides specific volume and internal energy and returns pressure, temperature, and sound velocity. EQ is also used for returning slip plane variables (NCALL=3).

REAL*8 SDEV: array of dimension five. Transfers stress deviator components. The components are in the order listed below:

1: $\sigma\ddot{e}_{xx}$

2: $\sigma\ddot{e}_{yy}$

3: $\sigma\ddot{e}_{xy}$

4: $\sigma\ddot{e}_{zx}$

5: $\sigma\ddot{e}_{yz}$

Together with the pressure in EQ above we have a total of six components.

REAL*8 FD: array of dimension 3 by 3. The total deformation tensor.

REAL*8 FPI: array of dimension 3 by 3. The inverse of the plastic deformation tensor.

REAL*8 EXC: array of dynamic dimension. The internal state variables are stored in this array. When the internal state variables are initialized (NCALL=1), the total space in REAL*8 words used up in EXC is returned in IERR.

REAL*8 HEPS: returns Hillís equivalent plastic strain.

REAL*8 PCUT: pressure tension cutoff. The use of this argument and S below depends on the elastic model.

REAL*8 S: array. The dimension depends on the elastic model. Contains parameters for the elastic model. For L2D S contains the parameters for pressure equation of state plus the shear modulus for the stress deviator model.

REAL*8 EXM: array of dynamic dimension. The parameters for the slip plane model are stored in this array. When the model parameters are read in (NCALL=0), the total space in REAL*8 words used up in EXM is returned in IERR.

CHARACTER*8 LABEL: array of dynamic dimension. The user input labels for the material parameters (NCALL=0) are sent to FRAGB in this array.

REAL*8 RLABEL: array of dynamic dimension. The values corresponding to the LABELs above are sent to FRAGB in this array.

INTEGER JPOSN: array of dynamic dimension. Indicators, indices, and the like associated with LABEL and RLABEL are sent to FRAGB in this array. For example, the following user input, "SNORMAL(2) = 0.3" would result in LABEL = "SNORMAL", RLABEL = 0.3, and JPOSN = 2.

INTEGER LM3: the array position in LABEL, RLABEL, and JPOSN that is now processed. Ordinarily LM3 is 1 upon entry of FRAGB. However, if the FRAGBED input is part of a larger free format input, LM3 might be non-trivial.

INTEGER NUM: the maximum value for LM3, i.e., the total number of free format input items.

The FRAGB routine reads in the material model parameters, initializes the internal state variables, and does part of the stress computations.

The first step in the stress computation is to call routine FRAGE that calculates the elastic stresses given a certain plastic deformation tensor. Next, routine FRAGY is called to check for

slip on the slip planes. If there is slip, FRAGY iterates for a plastic deformation tensor that fulfills the slip condition on all planes. During this iteration, FRAGE is called repeatedly from within FRAGY.

The slip will limit shear stresses but will not limit hydrostatic tension. The routine FRAGC is called to check the normal stress for tension on each plane. If the normal tension exceeds the cohesion on the plane, the pressure is reset to push up the normal stress on the plane. The pressure is not reset if it is already compressive. The slip adjusts the stress deviators, so there should only be need for adjustment of the pressure if the pressure is tensional.

Thereafter the comminution equation is solved. Finally the dislocation transport is done. The neighbor cell values needed for the transport were stored in arrays local to FRAGB by a previous call to load the transport variables (NCALL=4).

FRAGB also responds to various service calls, e.g., NCALL=3, 6, 10 above.

Hill's equivalent plastic strain is ordinarily defined as the summation of the square root of the second invariant of the plastic strain increment. Having a finite deformation tensor, we define Hill's equivalent plastic strain instead as the square root of the second invariant of the plastic strain tensor.

The comminution constitutes an ordinary differential equation with one unknown variable, the block size, and one independent variable, the driving stress. The problem with solving the equation numerically is that, for a certain range of the driving stress, the block size varies very rapidly. For other ranges of the driving stress, it does not vary at all. Because we know that the block size varies monotonically (it always decreases), a solution method with a variable time step is the best approach.

When the block size varies, we must subiterate on the comminution equation over the global time step (of the Lagrangian simulation). We start with a time step equal to the global time step.

We take a trial increment. If the block size decreases by more than a factor of two, we decrease the time step by a factor of two and try again. If the decrease in the block size is less than 0.1%, we have a good increment and we take the next trial increment.

If the change in the block size is between those two limits, we calculate the mean of the old and new block size, Bmn, and use this mean to calculate the new driving stress and the new width of the transition. The increment in the block size is a function of these two variables. We therefore want the driving stress and the transition width to be time centered between the old and the new time step level. We then go back and increment the block size with these mean values. We finally check that the resulting block size is smaller than or equal to Bmn above. If it is not, we cut the time step in half and do the trial increment over again. This maniac check is important when the block size varies very quickly.

If for a good increment the decrease in the block size is less than 1%, we increase the time step by 50% on the next trial increment.